



PCCP

**Role of Hydrogen Bonding in Bulk Aqueous Phase  
Decomposition, Complexation, and Covalent Hydration of  
Pyruvic Acid**

Journal:	<i>Physical Chemistry Chemical Physics</i>
Manuscript ID	CP-ART-08-2022-003579.R1
Article Type:	Paper
Date Submitted by the Author:	01-Oct-2022
Complete List of Authors:	Barquilla, Michael Dave; University of Massachusetts Dartmouth, Chemistry and Biochemistry Mayes, Maricris; University of Massachusetts Dartmouth, Chemistry and Biochemistry

SCHOLARONE™  
Manuscripts

# **Role of Hydrogen Bonding in Bulk Aqueous Phase Decomposition, Complexation, and Covalent Hydration of Pyruvic Acid<sup>‡</sup>**

**Michael Dave P. Barquilla and Maricris L. Mayes\***

Department of Chemistry and Biochemistry, University of Massachusetts Dartmouth, North  
Dartmouth, MA 02747, USA

\*Corresponding author:

E-mail: [mmayes@umassd.edu](mailto:mmayes@umassd.edu)

ORCID. 0000-0003-1184-7226

## ABSTRACT

Pyruvic acid (PA) is a model for amphiphilic oxygenated organic compounds, and together with its hydrogen-bonded (H-bonded) water complexes, their presence can alter atmospheric aerosol formation. However, the fundamental understanding of PA reaction mechanisms in different environments is still being debated. Here, the role of H-bonding on PA's degradation, complexation, and covalent hydration in bulk aqueous phase is investigated theoretically. Using CCSD(T)-F12/aug-cc-pVDZ-F12 on B2PLYP-D3BJ structures with solvation model based on density, we revealed the stabilization by intramolecular H-bonding of an intermediate, PA hydrogen-transferred tautomer, altered the PA degradation mechanisms compared to gas phase. We also found that the intramolecular H-bonding in the most stable gas phase conformer (Tc) is weakened due to bulk solvation, leading to slower acetaldehyde production rate. Natural bond orbital analysis characterized the primary intermolecular H-bond in PA-water complexes as electron donation of  $O_{\text{water}}$  lone pair ( $p$ ) to  $\sigma^*$  orbital of the OH group of PA. Stronger H-bonding is correlated to  $p$  to  $\sigma^*$  interaction, wider OH-O angles, and larger differences in the H-bond lengths between phases. Less charge difference on H-bonded atoms also indicates aggressive competition of H-bonding with solvation. Water's cooperative behavior was observed by lowering the water-complexed 2,2-dihydroxypropanoic acid (DHPA-H<sub>2</sub>O) barrier from PA-water complexes compared to DHPA in both phases, stabilizing the transition state and product with intermolecular H-bonding. PA is vital in atmospheric keto-acid chemistry; thus, changes in PA reaction mechanisms in different environments due to H-bond behavior will affect aerosol formation.

## 1 Introduction

The earth's atmosphere can be significantly altered by the presence of amphiphilic oxygenated organic compounds (AOOCs) formed from the photo-oxidation of volatile organic compounds such as isoprene, posing a threat to human health and climate change.<sup>1</sup> Different species of these molecules can clump together into larger gas-phase clusters and nanometer-sized aerosol particles in a critical atmospheric mechanism known as new particle formation.<sup>2</sup> At low atmospheric altitudes, water plays a more crucial role in these nucleation events,<sup>3,4</sup> forming wet aerosols that serve as cloud condensation nuclei. At the molecular level, hydrated complexes of AOOCs are formed as precursors to these clusters, which are thermodynamically stabilized by intermolecular interactions such as hydrogen bonding (H-bonding).<sup>5</sup> In pre-existing aqueous particles, H-bonding between AOOCs and water molecules at the air-water interphase may reduce the surface tension of the particles, enhancing cloud formation.<sup>6</sup> To make atmospheric chemistry more intricate and complicated, AOOCs can be photodegraded<sup>7</sup> and/or further react with other compounds present in the atmosphere, producing less volatile products.<sup>8,9</sup> These products consequently partition to gas-phase particles<sup>8-10</sup> or dissolve into the bulk aqueous phase within the aerosols.<sup>9-13</sup> Also, due to the inherent asymmetric nature of molecular composition, orientation, and density in aerosols,<sup>14,15</sup> especially at low atmospheric altitudes where water concentration is high, reactions within the air-aqueous boundary<sup>16,17</sup> vary greatly compared to gas phase or bulk aqueous phase. A comprehensive understanding of the atmospheric molecular complex formation in different environmental scenarios via H-bonding is imperative to give insight into the initial stages of new particle formation, which influences cloud properties. Furthermore, the disparity of the AOOC reactions in gas, bulk aqueous, and

interphase is still not entirely elucidated because studies are limited to the variability of atmospheric factors and reacting species; hence, theoretical characterization is needed.

Over the years, particular attention has been focused on pyruvic acid (PA), which is an excellent model for AOOCs since it contains both ketone and carboxyl functional groups. PA is the predominant photoproduct of isoprene<sup>18,19</sup> and serves as a core intermediate in atmospheric keto-acid chemistry.<sup>20–22</sup> It is naturally abundant in gas<sup>18,19,23–25</sup> and aqueous phase,<sup>20,22</sup> as well as in aerosols,<sup>21,26</sup> sea sprays,<sup>27–29</sup> and polar ice.<sup>30–32</sup> It is known to absorb in the near-UV region, decomposing to different photolytic products such as acetaldehyde<sup>33–36</sup> and acetic acid<sup>37–40</sup> in the gas phase. Photolysis is the main degradation sink of PA in the atmosphere as it reacts slowly with OH radicals,<sup>41</sup> and the major pathway involves decarboxylation towards methylhydroxycarbene (MHC),<sup>42,43</sup> which rearranges to acetaldehyde, the dominant product.<sup>44</sup> The success of this pathway is attributed to the strong intramolecular H-bonding between carboxylic hydrogen and ketonic oxygen, which anchors the H atom for the eventual transfer to the keto group via the H-chattering mode in the vibrationally hot  $S_0$ .<sup>45</sup> In the bulk aqueous phase, different scenarios dictate the fate of PA. Conformational switching between PA conformers becomes relevant in the aqueous phase as another conformer lacking the important intramolecular H-bonding becomes dominant when water concentration increases.<sup>46</sup> This decreased the branching ratio of the major photolytic product and reduced the photolysis rates.<sup>46</sup> It has also been confirmed that the photolysis of PA in bulk aqueous is possible even at lower photodegradation energies compared to the gas phase.<sup>47</sup> Acetic acid is also the dominant product alongside CO evolution in PA aqueous photolysis.<sup>47</sup> Different products obtained from the reactions of PA within the air-aqueous boundary<sup>12,13,48</sup> also further

differentiate the reaction mechanisms from gas and bulk aqueous phase. After photolysis, PA is also known to form a dimer in the aqueous and gas-water interface,<sup>48,49</sup> produced as nascent radicals, generating high molecular aggregates of organic compounds through oligomerization.<sup>12,48–52</sup> These disparities between gas, aqueous and interfacial photolysis of PA implicate distinct degradation mechanisms and must be differentiated from one another to understand aerosol formation in different environments fully.

The speciation of PA into its covalently-hydrated form, 2,2-dihydroxypropanoic acid (DHPA), and their respective deprotonated forms is another important scenario that could happen in the aqueous phase. Contrary to PA, DHPA does not absorb at solar wavelengths and is therefore not considered photoactive,<sup>53,54</sup> consequently offsetting the balance of atmospheric species that affect aerosol formation. The population distribution of these species depends on the pH of the environment<sup>32,53–58</sup> and plays a major role in the chemistry of sea sprays, where the pH of the bulk ocean is basic (pH  $\approx$  8),<sup>59,60</sup> and aerosols, fog, and cloud formation, which are usually very acidic (pH  $\approx$  0 to 5).<sup>53,61–66</sup> It is also reported that the air/water interphase has enhanced acidity over the bulk aqueous phase,<sup>67</sup> resulting in different photolytic products from the gas and bulk aqueous phase.<sup>13</sup> Computational characterization of PA degradation and DHPA formation in the bulk aqueous phase has not been investigated extensively due to the limitations of solvation calculations. Interestingly, covalent hydration of PA to DHPA is found to be dominant in water-restricted environments such as gas and particle-phase or nonpolar medium than in the highly water-concentrated environment (high humidity or bulk aqueous phase).<sup>55</sup> The ocean surface is known to concentrate nonpolar organic byproducts, creating a film that serves as a water-restricted medium for nonpolar reactions.<sup>68,69</sup>

Observation of more PA-water complexes alongside DHPA in a water-restricted environment implicates that these H-bonded complexes are important precursors for covalent hydration, necessitating further investigation.<sup>55</sup>

The common ground on PA's fate in gas and the aqueous phase is the role of both intramolecular and intermolecular H-bonding on conformational switching, decomposition, and hydration. The bulk solvent stabilization on PA conformers and isomers affects the strength of intramolecular H-bonding and their energies. In this paper, we contribute to understanding the fate of PA in different atmospheric environments, which consequently affect aerosol formation. We present the degradation mechanism of PA in bulk aqueous phase and compare the potential energy surfaces (PES) of different degradation channels, temporal dependence of species concentration, and rates of reactions with the previous gas phase study.<sup>44</sup> We describe the relationship between the strength of H-bonding through geometric features, atomic charges, and the thermodynamic properties of PA conformers and PA-water complexes in gas and bulk aqueous phases. We also present the relationship between the free energy change ( $\Delta G$ ) and H-bond strength to determine how DHPA formation proceeds from PA-water complexes in both phases. The  $\Delta G$  upon hydrogen bond formation is a good thermodynamic measure of the overall stability of hydrogen-bonded complexes.<sup>70</sup> Lastly, we provide new insights on how PA decomposition, complexation, and hydration in the gas phase differ from the bulk aqueous phase.

## 2 Methods

For the bulk aqueous phase, all equilibrium structures for the reactants, intermediates, transition states, and products along PA degradation PES, PA-water complexes, and species along

PA hydration were calculated using density functional theory with Grimme's atom-pairwise dispersion corrected (with Becke-Johnson damping) double-hybrid functional B2PLYP-D3BJ,<sup>71,72</sup> using aug-cc-pVTZ<sup>73</sup> basis set in solvation model based on density (SMD)<sup>74</sup> method. Transition states were validated by performing intrinsic reaction coordinate (IRC) calculations. Relative enthalpies were calculated using the electronic energies from coupled-cluster iterative single, double, and perturbative triple excitations with explicit exponential correlation<sup>75</sup> [CCSD(T)-F12] using aug-cc-pVDZ-F12<sup>76</sup> on B2PLYP-D3BJ structures. The reaction energetics were corrected for zero-point energy and Grimme's dispersion. The thermodynamic properties for the complexation and hydration reactions, such as reaction enthalpy ( $\Delta H$ ), entropy ( $\Delta S$ ), and Gibbs free energy ( $\Delta G$ ), were calculated at 1 atm and 298.15 K using the same method described above for single-point energies. Natural Bond Orbital (NBO) analysis<sup>77</sup> was used to determine the charges and orbital interactions of the PA conformers and complexes. For the gas-phase counterpart, the method described in the previous work was incorporated.<sup>44</sup> All electronic structure calculations employed ORCA<sup>78</sup> electronic structure package, version 4.2.1.

The microcanonical coefficients from the Rice-Ramsperger-Kassel-Markus (RRKM) theory were calculated to show the temporal dependence of each species in aqueous PA decomposition PES. Beyer-Swinehart algorithm<sup>79</sup> for the direct counting for harmonic oscillators was used to obtain the sums and densities of states, and the temporal dependence of each species was evaluated up to 100 000  $\text{cm}^{-1}$  at 1  $\text{cm}^{-1}$  increment. The reaction time was set to 100 fs with PA initial concentration set to 1. The product branching ratio of acetaldehyde and acetic acid was calculated at the reaction completion (1 s). The calculations were based on RRKM work done by Mansell et al.<sup>80</sup> using Mathematica 12.0.<sup>81</sup>

The frequencies obtained from SMD-B2PLYP-D3BJ//aug-cc-pVTZ were used to calculate the thermal rate constants of PA direct decomposition channels using KiSTheLP, version 2019.<sup>82</sup> The single-point energies used were from SMD-CCSD(T)-F12/aug-cc-pVDZ-F12 on the aqueous equilibrium geometries. The Lennard-Jones (LJ) parameters for PA were estimated to be  $\sigma = 5.46$  Å and  $\epsilon/k = 541$  K from empirical equations based upon additive volume increments and estimated boiling points, respectively.<sup>83,84</sup> The effects of solvation were assumed to be incorporated in the vibrations and the energies calculated by SMD in all the statistical kinetic calculations in the aqueous phase. The LJ parameters for H<sub>2</sub>O as the diluent for the aqueous-phase calculation were  $\sigma = 2.710$  Å and  $\epsilon/k = 506.0$  K.<sup>85</sup> The effect of pressure on the RRKM rate constants was evaluated between 1 to 760 torr at 0.10 torr increment for 400-1000 K at 100 K interval. The transition state theory with Wigner tunneling and unsymmetrical Eckart potential barrier tunneling corrections were used for the rates of DHPA and DHPA-H<sub>2</sub>O formation. All rate calculations were sustained at 1 atm, and the Arrhenius plots were constructed between 400-1000 K.

### 3 Results and Discussion

#### 3.1 Effect of bulk solvation on PA conformers and isomers

The most stable gas-phase PA conformer had been shown to contain a strong intramolecular H-bonding between the hydrogen of the carboxyl group ( $H_{\text{carboxyl}}$ ) and the oxygen of the carbonyl group ( $O_{\text{carbonyl}}$ ).<sup>44-46,55</sup> The other conformers were suggested to contain a weaker intramolecular H-bonding between the carboxylic oxygen and hydrogen.<sup>45,46,55</sup> A polarizable continuum model (PCM) study by Kakkar et al. showed that PA conformers and other isomers vary slightly in bond lengths in bulk solvation.<sup>86</sup> Explicit incorporation of water on

PA in gas phase calculations showed that the elongation of the intramolecular H-bonding is due to its disruption by forming intermolecular H-bonding with water.<sup>46,54,55,87,88</sup> These changes affected the energy differences between the conformers and were implicated as the reason for the difference in conformer distributions of PA in gas and bulk aqueous phase.<sup>45,46</sup> As an improvement from the previous PCM bulk solvation calculations,<sup>86</sup> SMD was used in this study to simulate not only the electrostatic interactions and the short-range interactions between the polar regions of PA and the water dielectric continuum in the first solvation shell but also the non-electrostatic effects of cavitation (energy needed to accommodate the solute in the solvent), dispersion (dispersion energy change upon dissolution), and changes in the solvent structure (entropic and energetic effects from structural changes in the solvent).<sup>74,89</sup> The structural changes caused by continuum models are significant for molecules containing intramolecular H-bond.<sup>90</sup> This is because the concomitant appearance of surface charges opposite to the polar sites weakens the intramolecular H-bond by crudely mimicking solute-solvent H-bonds. Here, we further characterized the cause of these changes by looking at the orbital interactions and charges calculated by NBO. We focused on the charges of oxygen atoms since these are electronegative atoms prone to be attacked by water to form intermolecular hydrogen bonding. The orbital interactions on the intramolecular H-bonding of PA conformers and isomers were characterized to see how bulk solvation affects these bonds' stability.

**Structures and charges.** The gas phase structures<sup>44</sup> of three PA conformers containing intramolecular H-bonding, which are labeled according to C<sub>methyl</sub>-C<sub>keto</sub>-C<sub>acid</sub>-O<sub>hydroxyl</sub> (upper case C = cis, T = trans) and C<sub>keto</sub>-C<sub>acid</sub>-O-H (lower case) angles (Fig. 1), six enol isomers from keto-enol isomerization of PA (Fig. 1), and four  $\alpha$ -lactone isomers (Fig. S1A) were optimized under SMD

bulk aqueous potential. Only the PA conformers and enol isomers were found to be stable in the aqueous phase, all of which have similar structural discrepancies compared to the gas phase (Fig. 1). Upon solvation, all double bonds bearing carbonyl and carboxylic oxygen atoms,  $C_{\text{carbonyl}}-C_{\text{carboxyl}}$ , and all OH bonds were elongated, whereas all the carboxylic C-OH bonds were shortened (Table S1A). These consequently stretched the intramolecular H-bonds slightly compared to the gas phase (Fig. 1), consistent with previous studies.<sup>46,86</sup>

In the aqueous phase, NBO calculations showed more negative charges on the oxygen atoms, particularly on doubly-bonded oxygen atoms (e.g., Tc's  $O_{\text{carbonyl}}$ : -0.52 (aqueous) vs. -0.47 (gas), Fig. 1), suggesting that the structure changed to accommodate more stabilization of polar regions by the solvent continuum. The slight increase in H-bond lengths (e.g., Tc's H-bond length: 2.062 (aqueous) vs. 2.022 Å (gas)) optimized the interaction of the electron donor (oxygen) and acceptor (OH group) of PA and enol isomers to the solvent surface charges. Looking closely at the charge difference upon solvation, the oxygen atom involved in H-bonding has a slight change compared to doubly-bonded oxygen atoms free of H-bonding. Also, the charges on H atoms are slightly more positive upon solvation, but no significant change in the enol<sub>a</sub> and enol<sub>b</sub>'s  $H_{\text{hydroxyl}}$  strongly involved in H-bonding. This implies a competition between intramolecular H-bonding and solvation in charge stabilization.

The aqueous phase led to the ring-opening of the triple-membered ring of the gas phase  $\alpha$ -lactone isomers (Fig. S1A)<sup>44,91</sup> forming PA hydrogen-transferred (PAHT) tautomers (Fig. 1) due to solvent stabilization of the oxygen atoms of the carboxylate group, delocalizing the lone pairs between the two. PAHT tautomer was previously calculated;<sup>86</sup> PAHT<sub>c</sub>, which contains a strong intramolecular H-bond (Fig. 1), was found to be crucial in gas phase excited state

degradation.<sup>92</sup> This tautomer had also been implicated as an important intermediate for the interconversion of pyruvate and its reduced form, lactate.<sup>93</sup> Lactate was argued to be always the end product of glycolysis.<sup>94–97</sup>

**Orbital interactions.** NBO analysis of the orbital interactions within the intramolecular H-bonds of PA conformers and enol isomers showed that Tc, enol<sub>a</sub>, enol<sub>b</sub>, and enol<sub>f</sub> contain the stronger kind of H-bonds which are characterized by electron donation of oxygen lone pair ( $p$ ) to the  $\sigma^*$  orbital of the opposite OH group (Table 1). PAHT<sub>c</sub> also exhibited this strong H-bonding between O<sub>carboxylate</sub> and the transferred H atom. These conformers also showed OH-O bond angles closer to 180° (Table S1A), enabling the oxygen  $p$  orbital to efficiently overlap with the  $\sigma^*$  orbital of the opposite OH group. Other conformers and isomers (including enol<sub>a</sub>) contain a weaker intramolecular H-bond within the carboxylic group, which involves an electron donation of the  $\sigma$  orbital of OH group to the  $\pi^*$  orbital of the opposite C=O (Table 1). This is not a typical H-bond donor-acceptor interaction and would be considered more as a dipole-dipole interaction. This is because the OH-O bond angle (Fig. 1) is so acute ( $\ll 180^\circ$ ) that the oxygen  $p$  orbital cannot properly overlap with  $\sigma^*$  orbital of the opposite OH group. This, in turn, led to the utilization of  $\sigma$  to  $\pi^*$  interaction. This classification of the type of H-bonding on these conformers is also supported by the charge difference of oxygen and hydrogen atoms discussed previously. The stabilization energies of the stronger H-bonds were lower in the aqueous compared to gas phase, but no significant change for the weaker H-bonds (Table 1). We note that these doubly-bonded oxygen atoms in the weaker intramolecular H-bonds were still stabilized by bulk solvation, as seen by the elongation of the H-bond length and the more negative charges on the oxygen. This suggests that the H-bond strength directly correlates to

the type of orbital interaction. H-bonds containing  $p$  to  $\sigma^*$  interaction is much stronger than  $\sigma$  to  $\pi^*$  interaction. However, the  $p$  to  $\sigma^*$  interaction is significantly weakened by bulk solvation compared to  $\sigma$  to  $\pi^*$  interaction.

**Conformational energies.** In gas phase, the lowest energy PA and enol conformers are Tc and enol<sub>a</sub>, respectively. These conformers contain the strong intramolecular H-bond, forming a five-membered ring and wider OH-O angles (Fig. 1) that makes the oxygen  $p$  orbital efficiently overlap with the  $\sigma^*$  of the opposite OH group (Table 1). Upon solvation, these structures were greatly destabilized since the intramolecular H-bond is disrupted to accommodate the stabilization brought by solute-solvent interaction. This resulted in the conformers' reordering and affected the aqueous phase's conformational switching. The greatest solvent stabilization was observed for enol<sub>c</sub>, which does not contain the two types of intramolecular H-bonds mentioned earlier (with relative enthalpies from 16.88 kcal/mol in gas to 2.13 kcal/mol in the aqueous phase). This clearly shows an aggressive competition between water molecules/bulk potential and intramolecular H-bonding on stabilizing the oxygen atoms.

These observations imply that the intramolecular H-bond is weaker in the aqueous phase due to the preferential stabilization of the polar atoms with the bulk solvent. In comparison, a stronger intramolecular H-bond was observed in the gas phase since internal stabilization of the oxygen lone pairs is forced in the absence of a hydrophilic environment. The previous study suggested that the intramolecular H-bond is needed for PA photolysis to proceed in the gas phase since it reinforces the H-chattering mode between H<sub>carboxyl</sub> and O<sub>carbonyl</sub>, leading to eventual H-transfer and decarboxylation to acetaldehyde.<sup>45</sup> However, the effect of disrupting this H-bond via intermolecular H-bonding with water is the reduction of the

photolysis rate of PA where it was shown that Tt dominated the conformer distribution over Tc in the aqueous phase.<sup>46</sup>

### 3.2 Thermal decomposition pathways of PA in bulk aqueous phase

The previous computational gas phase study<sup>44</sup> on PA confirmed that the dominant acetaldehyde production channel is through the MHC-CO<sub>2</sub> intermediate. It also showed additional pathways such as the direct acetic acid conversion, MHC-CO<sub>2</sub> to acetaldehyde, and MHC-CO<sub>2</sub> to vinyl alcohol, providing a more detailed picture of PA degradation in the gas phase. The decomposition channels of PA in aqueous phase were mapped based on the previously calculated pathways in gas phase.<sup>44</sup> Due to the appearance of PAHT tautomers in the aqueous phase and the absence of lactone isomers, new pathways in the unimolecular degradation of PA were characterized (Scheme 1) compared to the gas phase.<sup>44</sup> The bulk solvation stabilized PAHT<sub>c</sub> with a strong intramolecular H-bonding (Table 1), which split the asynchronous H-transfer and C-C bond cleavage in the concerted MHC-CO<sub>2</sub> and vinyl OH-CO<sub>2</sub> production and the concerted double proton shift of enol<sub>b</sub> production in gas phase<sup>44</sup> into two succeeding processes in aqueous phase. No transition state structures were found in rotating the C-OH bond to convert PAHT<sub>c</sub> to other tautomers, which supports the strength of the intramolecular H-bonding within PAHT<sub>c</sub>. On the other hand, the gas phase enol to vinyl OH-CO<sub>2</sub> conversion pathway<sup>44</sup> was also not found in aqueous phase.

**Conformational switching.** Shown in Fig. 2 is the PES of PA degradation in the aqueous phase. The structures of minima and saddle points are shown in Figs. S2A and S3A, respectively. The saddle point structures of conformational switching between PA conformers and other isomers (enol and PAHT) are shown in Fig. S4A. The conformational switching of PA to other

conformers was included since PA photolysis in the aqueous phase is suggested to be slowed down by conversion of Tc to Tt due to the elongation of Tc's internal H-bond.<sup>46</sup> Aside from lower relative energies of Tt and other conformers compared to Tc, lower energy barriers between these conformers (TS-a1 and TS-a2 in Fig. 2) were calculated in the aqueous phase compared to gas. Cc conformer was also found to be a true minimum in aqueous phase due to solvent stabilization.

**Enol isomerization.** Like PA conformers, the energetics of enol isomers were changed significantly by bulk solvation, leading to much closer relative energies. They have lower barriers for switching between enol<sub>a</sub>, enol<sub>b</sub>, and enol<sub>c</sub> (Fig. 2), which are the important intermediates in acetic acid production from PA (via TS3→TS5→TS-c2→TS4→TS-b→TS2 pathway in Fig. 2). Tc can produce enol<sub>f</sub> via TS5a (Fig. S3A), which can switch to enol<sub>e</sub> and enol<sub>d</sub> (Fig. S5A). But, unlike the gas phase,<sup>44</sup> the transition states connecting enol<sub>d</sub> to enol<sub>a</sub> and enol<sub>c</sub> were not found in the aqueous phase (Fig. S5A). Therefore, acetic acid production through enol isomers can only proceed through isomerization of Tc to enol<sub>b</sub>, which is split into two processes via PAHT<sub>c</sub> in aqueous phase through TS3 and TS5 (Fig. 2). The production of enol depends on the availability of PAHT<sub>c</sub>, which is also consumed to produce MHC-CO<sub>2</sub> (TS7) and vinyl OH-CO<sub>2</sub> (TS6).

**PAHT production.** PAHT<sub>c</sub> production has a shallow energy barrier (TS3), meaning Tc can readily convert into this intermediate to feed the other processes. However, the reverse energy barrier is also shallow, which means this can revert to Tc, adding to the competition of its consumption. Compared to the energy barrier of lactone production in the gas phase<sup>44</sup> (TS3, 35.49 kcal/mol), the PAHT<sub>c</sub> production barrier is much lower (13.27 kcal/mol). However, no

direct interconversion pathways were found towards PAHT<sub>a</sub> or PAHT<sub>b</sub>; thereby, switching between PAHT tautomers must go through enol production first (via TS5→TS-c2→TS4→TS-b in Fig. 2).

**Acetic acid production.** Energy barriers toward acetic acid production in the aqueous phase are lower than gas-phase barriers (TS1, TS2, TS3, TS4, and TS5). Acetic acid production in the aqueous phase only has two routes, via direct conversion (TS1) or PAHT<sub>c</sub> (via TS3→TS5→TS-c2→TS4→TS-b→TS2 pathway). But, there are three in the gas phase:<sup>44</sup> direct conversion from T<sub>c</sub>, conversion via lactone, and enol production. It should be noted that the endpoints of TS2, TS3, TS4, and TS5 are different in the gas phase since lactone is replaced by PAHT tautomers in the aqueous phase. However, these barriers are compared since the imaginary modes of the transition states are similar, except for TS3 which is compared because lactone and PAHT intermediates are similar in structure.

**Acetaldehyde production.** In contrast to acetic acid production, all energy barriers leading to acetaldehyde production were similar (TS8) or slightly higher (TS7, TS9, TS10, and TS11) in the aqueous phase compared to gas phase, except for the PAHT<sub>c</sub> to vinyl OH-CO<sub>2</sub> conversion (TS6), which is a concerted T<sub>c</sub> conversion in the gas phase.<sup>44</sup> The disappearance of enol to vinyl OH-CO<sub>2</sub> pathway reduced the number of channels towards acetaldehyde. It is also noteworthy that the most crucial channel in the gas phase, via MHC-CO<sub>2</sub> production, has a higher energy barrier in aqueous phase, and it is split into two processes via PAHT<sub>c</sub>. Overall, the PES landscape of PA degradation in aqueous phase is significantly distinct from the gas phase.

### 3.3 Temporal dependence of PA degradation species in aqueous phase

Fig. 3 depicts different snapshots of the concentrations of the species in aqueous phase, limited within 100 fs timescale at increasing internal energies in contrast to previous gas phase results.<sup>44</sup> These were calculated using the differential rate equations with RKKM microcanonical coefficients of each species based on the kinetic pathways built from Scheme 1 and Fig. 2. In the aqueous phase, the degradation opened at  $15\,400\text{ cm}^{-1}$  ( $\sim 44.03\text{ kcal/mol}$ ), in which more than 70% of Tc switched to its other conformer, Tt. In comparison, previous gas-phase calculations<sup>44</sup> showed that Tc degradation starts at  $13\,700\text{ cm}^{-1}$  ( $\sim 39.17\text{ kcal/mol}$ ), where the  $\alpha$ -lactone channel opens. The caveat in this comparison is that gas-phase degradation excludes PA conformational switching, which is based on previous studies showing PA photolysis in the gas phase is only attributed to Tc conformer<sup>45,46</sup> while in aqueous phase, abundance of Tt is more significant<sup>46</sup> and thus switching is allowed in aqueous phase calculations. In both gas and aqueous phase, enol conformers exhibited minimal build-up all throughout the internal energy assessed as these intermediates were constantly consumed.

At  $34\,000\text{ cm}^{-1}$  (Fig. 3 top left), Tt conformer was consumed down to 50% as the build-up of Ct conformer was up to 12%, which consequently gave rise to Cc concentration reaching 7%. The decrease of Tc concentration (from 30% at the initial energy to 23%) also signified the opening of other channels, albeit slightly, with PAHT<sub>c</sub> concentration spiking to more than 5% at the onset of the reaction ( $<20\text{ fs}$ ) and minimal build-up of MHC-CO<sub>2</sub>, vinyl alcohol-CO<sub>2</sub> and other PAHT conformers below 5% at 100 fs. In gas phase (Fig. 3 top right), Tc concentration decreased to 50% at higher energy ( $40\,750\text{ cm}^{-1}$ ) but converted to significant amount of acetaldehyde, MHC-CO<sub>2</sub>, vinyl alcohol-CO<sub>2</sub>, and even acetic acid 100 fs.

At  $49\,000\text{ cm}^{-1}$  (Fig. 3 middle left), acetaldehyde reached 50% abundance, and acetic acid accumulated to almost 3% concentration while all four PA conformer abundances were within 5–10%. Important intermediates such as MHC–CO<sub>2</sub> and PAHT conformers stayed below 5% concentration. The sufficient internal energy drove the reaction towards the eventual product sinks, acetaldehyde, and acetic acid, or low reverse barrier height forced reverse rearrangement back to their respective precursors. Although at this energy, a significant spike in concentration (15%) was observed for MHC–CO<sub>2</sub> at the start of the reaction (<20 fs), attributed to higher exit channel barriers in aqueous phase. It is interesting to note that vinyl alcohol still lingered at a higher concentration (28%), which means it is one of the preferred channels in consuming PAHT<sub>c</sub>, competing against MHC–CO<sub>2</sub> production, enol conversion, and reverse reactions. Furthermore, it accumulated due to only having one exit channel (towards acetaldehyde) with considerable energy barrier height. In comparison to gas phase (Fig. 3 middle right), acetaldehyde concentration reached 50% at lower energy ( $43\,000\text{ cm}^{-1}$ ) while Tc was still significantly present (30%), and other species, including acetic acid, were below 10% build-up within 100 fs. Vinyl alcohol has a lower abundance in gas phase due to the high conversion barrier from Tc, while in aqueous phase, energy barrier from PAHT<sub>c</sub> is significantly lower. This means that acetaldehyde production was hindered in aqueous phase since species were trapped within low energy wells and barriers in the PES, interconverting reversely between low relative energy PA conformers, PAHT<sub>c</sub>, MHC–CO<sub>2</sub>, and enol isomers while in gas phase, well-defined barriers ensured production of acetaldehyde.

At  $54\,800\text{ cm}^{-1}$  (Fig. 3 bottom left), almost all the intermediates were consumed except for some PA species that remained trapped in conformational switching (<1%) at 100 fs. Acetic

acid retained minimal build-up (3%) while acetaldehyde dominated (75%). Significant vinyl alcohol remained (18%) at 100 fs. In gas phase with the same energy input (Fig. 3 bottom right), all of Tc was converted to the dominant acetaldehyde and the minor acetic acid products, reaching steady-state concentrations of 85% and 14% at 100 fs, respectively and a small build-up of vinyl alcohol at 1% was observed. Compared to gas-phase degradation, longer reaction time was needed to decompose all PA conformers in aqueous phase. Fig. S6A shows steady-state concentrations of acetaldehyde (94%) and acetic acid (4%) were almost reached within 500 fs, while vinyl alcohol was consumed down to 2%. This supports previous work showing PA photolysis is slower in aqueous phase and needs more reaction time to reach steady state product concentrations.<sup>46</sup>

**Exit channel ratio.** The acetaldehyde to acetic acid ratio was evaluated between 20 000  $\text{cm}^{-1}$  to 100 000  $\text{cm}^{-1}$  at 1 s, where it is assumed that only the steady-state products are present, and all the intermediates are consumed. At the reaction completion, the maximum ratio of acetaldehyde to acetic acid in aqueous phase was 57.39 at 59 000  $\text{cm}^{-1}$  (Fig. S7A). This is significantly higher than gas phase ratio (8.17),<sup>44</sup> although achieved at higher energy (gas: 44 000  $\text{cm}^{-1}$ ). However, the aqueous phase product ratio is distinct from the gas phase,<sup>44</sup> with acetaldehyde production significantly dominating only within a window of energy ( $\sim 35\,000\text{--}75\,000\ \text{cm}^{-1}$ ) over acetic acid production. This is important in aqueous phase chemistry since dominant products may vary depending on the amount of energy acquired by the system, and this shows acetic acid may dominate over acetaldehyde at lower or higher energies, depending on the accessibility of solar radiation in a given environment. This also supports a previous study that shows acetic acid as the dominant product in aqueous photolysis.<sup>47</sup> Acetic acid may

dominate in bulk ocean surfaces where access to UV radiation is considerably lower compared to higher atmospheric altitude.

### 3.4 Thermal rate constants

**Fastest decomposition channel.** The rates of the main decomposition channels of Tc (towards Tt, PAHT<sub>c</sub>, direct acetic acid, and acetaldehyde formation) in aqueous phase were calculated using RRKM theory. The Arrhenius plots of the three-parameter expression of the least-squares fit (Table S2A) of the calculated RRKM rate coefficients of these channels were plotted within 400-1000 K in H<sub>2</sub>O diluent (Fig. 4A). Among the main reaction channels in the aqueous phase, Tc-Tt switching is the fastest within 400–625 K, followed by PAHT<sub>c</sub> formation until about 488 K when the MHC–CO<sub>2</sub> formation overtakes (Fig. 4A). These rates support the dominance of PA conformers and PAHT<sub>c</sub> at lower energies at the onset of temporal dependence calculations. The flatter slopes of Tc-Tt switching and PAHT<sub>c</sub> formation within the temperatures considered may indicate pressure fall-off effects since the high-pressure limit rates are not yet achieved as the temperature is increased.<sup>98</sup> This behavior is more distinct in pathways with low energy barriers, whereas pathways with high reaction barriers stay at high-pressure limit rates. The calculated E<sub>a</sub> in aqueous phase (Table S2A) for Tc-Tt switching (14.30 kcal/mol), PAHT<sub>c</sub> (19.45 kcal/mol), and MHC–CO<sub>2</sub> production (34.81 kcal/mol) are considerably low compared to direct acetaldehyde (75.60 kcal/mol) and acetic acid formation (52.01 kcal/mol). The Tc decomposition rates and E<sub>a</sub> follow the same trend, with acetaldehyde formation being the slowest, followed by acetic acid production until pressure fall-off effects occur at high temperatures, where the direct acetic acid pathway becomes the fastest. The direct

acetaldehyde pathway becomes faster than Tc-Tc switching and PAHT<sub>c</sub> formation at 1000 K (Fig. 4A).

A comparison of the rates of acetaldehyde, acetic acid, and MHC–CO<sub>2</sub> formation in gas and aqueous phases is shown in Fig. 4B. Direct acetaldehyde formation is faster in gas phase than in the aqueous phase while acetic acid production is faster in aqueous phase than in the gas phase, consistent with the temporal dependence and exit channel ratio calculations and previous experiments on aqueous PA photolysis.<sup>46,47</sup> At lower temperatures, gas and aqueous MHC–CO<sub>2</sub> production rates are similar, but as the temperature increases, the gas phase is faster than its aqueous counterpart. This is due to the negative temperature dependence (*n*) of the pre-exponential factor of the rate equation (Table S2A) in aqueous phase, making the aqueous MHC–CO<sub>2</sub> formation slower as the temperature increases. Also, it is dependent on the PAHT<sub>c</sub> production in aqueous phase.

**Effect of pressure.** The effect of pressure was explored to determine which of the direct decomposition channels of PA in aqueous phase goes to pressure fall-off regime as temperature increases. The rates were evaluated at 0–760 torr at 0.10 torr increment and 400–1000 K at 100 K interval (Fig. S8A). In this work, H<sub>2</sub>O was used as the buffer gas to simulate solvation. The early flattening of the Log *k*(s<sup>-1</sup>) vs. Log *P*(torr) curve at lower pressures suggests that the rates are at the high-pressure limit and already past the pressure fall-off regime.<sup>98</sup> This means that pressure has a minimal effect on the rate as the temperature is increased.

The direct acetaldehyde and acetic acid pathways stay within the high-pressure limit as the temperature increases due to their high energy barriers. On the other hand, low energy barrier pathways shift from high-pressure limit to either pressure fall-off regime or low-

pressure limit rates. For Tc-Tt switching and PAHT<sub>c</sub> formation, even at 400 K, the rates are at the pressure fall-off regime and go to low-pressure limit rates as the temperature increases to 1000 K. The MHC-CO<sub>2</sub> formation is still at the high-pressure limit up to 600 K and slides to the pressure fall-off regime at 700 K before returning to low-pressure limit rates at 1000 K.

Typically, rates at the high-pressure limit go faster as the temperature increases, as the forward rate would be higher than the recombination rate. However, the channels with low barriers that went back to the low-pressure limit need higher pressure of the bath diluent to achieve enough collision concentration for the forward rate to overtake the recombination rate as the temperature increases.<sup>98</sup> Thus, we see the lowering of the rates of Tc-Tt switching, PAHT<sub>c</sub> formation, and MHC-CO<sub>2</sub> formation at higher temperatures.

### 3.5 Formation of PA-water complexes in gas and aqueous phase

Preceding calculations of PA monomers (Fig. 1) in the bulk aqueous phase confirmed the weakening of intramolecular H-bonding compared to the gas phase due to the solvent stabilization of the oxygen atoms which consequently altered their respective relative energies. Further exploration of PA conformational switching in a water-rich environment was done by incorporating explicit water molecules and investigating the effect of the intermolecular interactions of water with PA in both gas and aqueous phase. Four different water interactions, specifically on the oxygen atoms of each PA conformer (except for Cc), were considered (Figs. S9A to S11A): in-plane orientations of water with H<sub>carboxyl</sub> (*orientation a*), lateral orientation parallel to the C<sub>carboxyl</sub>-C<sub>carbonyl</sub> plane (*orientation b*), between the carboxyl and carbonyl groups (*orientation c*), and between the carbonyl and methyl groups (*orientation d*). However, not all orientations were found to be a true minimum in some PA-water complexes.

**Water orientation in the lowest energy PA-monohydrated complexes.** Previous gas-phase theoretical studies showed that the lowest energy PA-monohydrated complexes (1 PA:1 H<sub>2</sub>O) involved the orientation of water disrupting the intramolecular H-bonding of the three PA conformers (PA-H<sub>2</sub>O<sub>a</sub> complexes).<sup>46,54,55,87,88</sup> This finding was reproduced in this study, where out of all the four orientations explored (Figs. S9A to S11A), *orientation a* of PA-H<sub>2</sub>O complexes has the lowest energy (Fig. 5 and Table S3A). Structurally, this orientation has the shortest H-bond length and has an OH-O angle closest to 180° (Table 2 and Table S4A. NBO calculations (Table 2) characterized a very strong intermolecular H-bonding (primary H-bond) with the lone pair of O<sub>water</sub> as electron donor to the  $\sigma^*$  of the opposite PA's OH group. A second, much weaker, intermolecular H-bond (secondary H-bond) also contributes, with the lone pair ( $p$ ) of the O of PA conformers (e.g., O<sub>carbonyl</sub> for Tc) as electron donor to the  $\sigma^*$  of OH in water. The other orientations only have the weaker interactions, either the  $p$  to  $\pi^*$  interactions for *orientation b* (Table S5B and S8B) or the secondary H-bond for Tc-H<sub>2</sub>O<sub>b'</sub> and *orientation c* and *d* for Ct and Tt (Table S6B, S9B, and S10B).

PA-water complexation is more likely to happen in bulk aqueous phase due to multiple possible water interactions with the oxygen atoms of PA. However, the intermolecular orbital interactions of these complexes in bulk aqueous have never been characterized before. Our results showed that even with the charge stabilization of the bulk aqueous potential on both PA and water subunits, disruption of intramolecular H-bond still produced the lowest energy PA-water complexes among the orientations on each of the conformers (Fig. 5 and Table S3A). NBO calculations showed similar dominant interactions for gas and aqueous phases (Table 2). The primary intermolecular H-bond lengths of all the PA-water complexes shortened, and the

corresponding OH-O angles became closer to  $180^\circ$  compared to gas phase (Table 2), while the secondary intermolecular H-bond weakened or totally vanished. These huge structural differences in aqueous phase compared to gas phase maximized the solvent stabilization of the charges of the polar regions on both PA and water subunits by breaking the weaker intermolecular H-bond while strengthening the primary H-bonding's orbital (Table 2).

**Conformational switching between PA-monohydrated complexes.** In gas phase, the PA-monohydrated complexes have closer relative energies compared to the PA monomers (Table 3), with Tc-H<sub>2</sub>O<sub>a</sub> as the lowest energy PA-water complex (Tc-H<sub>2</sub>O<sub>a</sub> < Tt-H<sub>2</sub>O<sub>a</sub> < Ct-H<sub>2</sub>O<sub>a</sub>). All three PA-water complexes have similar intermolecular H-bond lengths, but Tc-H<sub>2</sub>O<sub>a</sub> has the closest OH-O angle of the primary H-bond to  $180^\circ$ , followed by Tt-H<sub>2</sub>O<sub>a</sub>, then Ct-H<sub>2</sub>O<sub>a</sub> (Table 2 and Fig. 5). This means that aside from length, the OH-O angle is more important in determining the H-bond strength, enabling the proper overlap of the interacting orbitals. Consequently, a significant lowering of relative enthalpies is observed compared to PA monomers due to the formation of intermolecular H-bonds, compensating for the decrease in relative entropy brought by complexation (Table 3). This implies that lower relative energies are calculated for PA-water complexes with more stabilized OH group of PA.

In the aqueous phase, Tt-H<sub>2</sub>O<sub>a</sub> is the lowest energy PA-water complex, followed by Ct-H<sub>2</sub>O<sub>a</sub> and Tc-H<sub>2</sub>O<sub>a</sub> (Table 3), in contrast to the ordering of the relative energies in gas phase and PA monomers in aqueous phase. The main driving factor on stability is still the efficiency of the intermolecular H-bonding of PA's OH group, which is supported by more negative enthalpies calculated for these PA-water complexes compared to aqueous PA monomers (Table 3).

However, the slight advantage of the stabilization of Tt-H<sub>2</sub>O<sub>a</sub> over Ct-H<sub>2</sub>O<sub>a</sub> is that it has both

secondary interaction (weak  $p$  to  $\pi^*$ , Table S7B) and  $p$  to  $\sigma^*$  between  $O_{\text{carboxyl}}$  and  $OH_{\text{water}}$  (Table S4B). This also made the distance of  $O_{\text{carboxyl}}$  and  $H_{\text{water}}$  of Tt-H<sub>2</sub>O<sub>a</sub> slightly shorter compared to Ct-H<sub>2</sub>O<sub>a</sub> (3.232 Å < 3.248 Å, Table 2) and OH-O angle slightly higher (91.05° > 90.77°, Table 2).

**Conformational switching between PA-dihydrated complexes.** Another water molecule was added to the lowest PA-monohydrated complexes (Tc-H<sub>2</sub>O<sub>a</sub>, Tt-H<sub>2</sub>O<sub>a</sub>, and Ct-H<sub>2</sub>O<sub>a</sub>), forming PA-dihydrated complexes (1 PA:2 H<sub>2</sub>O), to study the effect of additional intermolecular H-bonding offered by more explicit water molecules to PA conformational switching in both gas and aqueous phase (Fig. 5). We limited the number of water molecules to two since the experiment by Maron et al.<sup>55</sup> only explored the connection of PA-water complexes to DHPA and DHPA-H<sub>2</sub>O. In the gas phase, the PA-dihydrated complexes follow the same trend as their monohydrated counterparts (Tc-2H<sub>2</sub>O < Tt-2H<sub>2</sub>O < Ct-2H<sub>2</sub>O, Table 3). Another dihydrate of Tc (Tc-2H<sub>2</sub>O' in Fig. S12A) was found previously,<sup>86,87</sup> but we found Tc-2H<sub>2</sub>O as the lowest energy dihydrate (Table S3A) which has  $OH_{\text{carboxyl}}-O_{\text{water}1}$  bond angle closest to 180° compared to the other dihydrates (Table 2). NBO analysis showed that the major orbital interaction of the strong intermolecular H-bond is still the electron donation of  $O_{\text{water}} p$  orbital to the  $\sigma^*$  orbital of the opposite PA's OH group (Table 2). Although Tt-2H<sub>2</sub>O has the least OH-O bond angle of the primary intermolecular H-bonds, it is the next lowest dihydrate in gas phase since the two water molecules also form a strong intermolecular H-bond between each other (additional 9.10 kcal/mol stabilization energy), which offers more stabilization of the oxygen atoms and, thus, stabilizes the whole complex (Table 2).

It should be noted that the structure of the Tt-2H<sub>2</sub>O complex is the same as what has been characterized before<sup>55,86</sup> where the C<sub>carbonyl</sub>-C<sub>carboxyl</sub> bond is twisted to accommodate the two water molecules. This structural rearrangement made the relative entropy lower but was compensated by the stabilization of oxygen atoms of water, thus lowering the relative enthalpy of the complex compared to the others (Table 3).

In aqueous phase, stabilization of the polar regions brought by bulk solvation affected the structures of the complexes compared to the gas phase. The weaker intermolecular H-bonds are less preferred in stabilizing the oxygen atoms compared to the bulk solvation, consequently breaking them in aqueous phase. Table 2 shows the weakening or disappearance of the secondary intermolecular H-bonds ( $p$  orbital of O<sub>carbonyl</sub> to  $\sigma^*$  OH<sub>water</sub> for Tc-2H<sub>2</sub>O<sub>a</sub> and Tt-2H<sub>2</sub>O and  $p$  orbital of O<sub>carboxyl</sub> to  $\sigma^*$  OH<sub>water</sub> for Ct-2H<sub>2</sub>O). This made the primary intermolecular H-bonds even stronger by shortening their distances compared to the gas phase and stronger stabilization energies of the primary intermolecular H-bonds (Table 2). This also made the main H-bond anchoring the second water molecule near Tc's methyl group and Ct's carbonyl and carboxyl groups slightly stronger (highlighted in gray in Table 2). The main driving factor on stability is still how effectively the orbitals of the strong intermolecular H-bonds overlap, especially on OH<sub>carboxyl</sub>. Ct-2H<sub>2</sub>O structure has OH-O bond angles of the strong intermolecular H-bonds closest to 180°, making it the lowest energy PA-dihydrate in aqueous phase, followed by Tc-2H<sub>2</sub>O and then Tt-2H<sub>2</sub>O. The stabilization energy of the strong intermolecular H-bond of water to the OH<sub>carboxyl</sub> of PA in Tt-2H<sub>2</sub>O did not change significantly upon solvation compared to other PA-dihydrates (Table 2), which consequently gave the highest relative enthalpy (Table 3) in aqueous phase.

**Factors affecting conformational switching.** Conformational switching between PA conformers and their hydrated complexes in gas and aqueous phase depends on how efficiently PA's carboxylic hydrogen is stabilized. In gas phase, strong intramolecular H-bonding on PA monomers stabilized the lone pair of the opposite doubly bonded oxygen (Fig. 1). In contrast, in aqueous phase, stabilization was brought by the elongation of intramolecular H-bond on PA monomers for more efficient bulk solvation (Fig. 1). The differences in the charges of oxygen and hydrogen atoms in PA complexes upon solvation also exhibit the same behavior as that on PA monomers and enol isomers (discussed previously), where the charges of oxygen and hydrogen atoms involved in the stronger type of intermolecular H-bonding is not as delocalized compared to the non-H-bonded ones (Figs S9A to S12A), indicating a competition of bulk solvation and H-bonding on charge stabilization. The strength of the intramolecular H-bond is also correlated to the type of orbital interaction (Table 1).

In both gas and aqueous phase, the strongest (primary) intermolecular H-bonding between PA-water complexes always involves electron donation of the  $p$  orbital  $O_{\text{water}}$  molecule to the  $\sigma^*$  orbital of the  $\text{OH}_{\text{carboxyl}}$  of PA. This was exhibited mainly by OH-O angles closer to  $180^\circ$  (Table 2). Secondary orbital interactions also added to the stability of PA-water complexes. Although the secondary interactions are of  $p$  to  $\sigma^*$  type of intermolecular H-bonding, electron donation from doubly-bonded oxygen atoms of PA to OH group of water is always significantly weaker than the primary intermolecular H-bond. These also have more acute OH-O angles (Table 2).

There seems to be no idiosyncratic dependency of the relative energies of PA-water complexes on the intermolecular H-bond length if they are compared directly. However, it was

found out in both PA-monohydrated and dihydrated complexes that lower relative energies with respect to its Tc-water complex in aqueous phase were calculated for PA-water complexes with the greatest differences in the H-bond lengths between phases ( $\Delta\text{distance} = \text{distance}_{\text{aq}} - \text{distance}_{\text{gas}}$ ) of the primary intermolecular H-bonding from gas to aqueous phase, specifically between  $\text{O}_{\text{water}}$  and  $\text{H}_{\text{carboxyl}}$  of PA (Table 2). Furthermore, contrary to what has been reported by the previous study,<sup>70</sup> significant lengthening of the weaker H-bonds upon solvation on PA-water complexes (Table 2) supports the proposed model<sup>99–101</sup> that water elongates H-bonds compared to aprotic environments, consequently decreasing the potential energy within the H-bond. This was also observed in the previous section for PA conformers and isomers upon solvation (Fig. 1).

**Complexation free energies of PA-water complexes.** The complexation of one water molecule is energetically favorable for Tt and Cc compared to Tc in gas and aqueous phases because stronger intramolecular H-bonding must be broken for Tc to form a water complex (Table 4). Although the free energies of complex formation of these three are much closer in aqueous phase due to the weakening of intramolecular H-bonding caused by solvent stabilization.

The free energies of complexation of the additional water molecule on the three lowest energy PA-monohydrated complexes are comparable to each other in gas phase since the complexation no longer involves breaking of intramolecular H-bonding of PA (Table 4). In the aqueous phase, the complexation of PA-dihydrated complexes is driven by overcoming the solvent stabilization of both PA and the already complexed water molecule to accommodate the new  $\text{H}_2\text{O}$ , resulting in much higher complexation free energies compared to gas phase. Tt–

$2\text{H}_2\text{O}$  is the least favorable to form in aqueous phase due to the twisting of the  $\text{C}_{\text{carbonyl}}-\text{C}_{\text{carboxyl}}$  destabilizing the whole complex (higher enthalpy of formation), while  $\text{Ct}-2\text{H}_2\text{O}$  and  $\text{Tc}-2\text{H}_2\text{O}$  have comparable complexation free energies.

In general, it is energetically favorable to complex water to PA in gas phase than in aqueous phase because solvent stabilization of the oxygen lone pairs of the conformers in aqueous phase is more significant over intermolecular hydrogen bonding. The more negative charge on oxygen atoms and more positive charge on hydrogen atoms upon solvation confirm the previous model<sup>102-104</sup> that lower  $\Delta G_{\text{formation}}$  is observed in relation to stabilized donor-acceptor groups in water complexes compared to aprotic solvents. This caused the enthalpies of complexation in aqueous phase to be higher, resulting in higher free energies of complexation than gas phase (Table 4). This supports the previous experiment by Maron et al. that detected more PA-water complexes in water-restricted environments.<sup>55</sup> Furthermore, PA-dihydrated complexes are less favorable energetically to complex than PA-monohydrated in both gas and aqueous phase. It is important to note that PA-water complexation is a crucial initial step in the covalent hydration of PA towards DHPA. Although complexation is more favorable in gas phase, intrinsic solvation is thermodynamically spontaneous, and thus, all the PA-water complexes are more stabilized in the bulk aqueous phase (Table S3A).

### 3.6 Covalent hydration of PA

**PA-water complexes as precursors to covalent hydration.** As the previous studies suggest, water concentration has a major role in DHPA formation.<sup>32,55,87</sup> For a water-restricted environment, intermolecular H-bonding of PA-water complexes is forced due to the absence of a hydrophilic environment. This PA-water complex formation resulted in large quantities of

DHPA.<sup>55</sup> Table 5 shows that it is more favorable to form DHPA and DHPA–H<sub>2</sub>O from PA-water complexes in gas phase than from separated Tc monomer and water molecule. Gas-phase IRC calculations confirmed that transition states leading to DHPA and DHPA–H<sub>2</sub>O are connected to Tc–H<sub>2</sub>O and Tc–2H<sub>2</sub>O, respectively, and DHPA–H<sub>2</sub>O formation is slower than DHPA formation.<sup>44</sup> Preceding results on free energies of complexation of PA-water complexes coincide with these findings, where PA-monohydrated complexes are slightly favorable to form compared to PA-dihydrated complexes in the gas phase (Table 4).

Interestingly, the starting Tc–H<sub>2</sub>O complex (Tc–H<sub>2</sub>O<sub>b</sub>') towards DHPA in gas phase<sup>44</sup> is not the lowest energy Tc–H<sub>2</sub>O complex calculated in this study (Fig. S9A and Table S3A). This orientation where water interacts with the methyl group of Tc is an important orientation in forming intermolecular H-bonded water cages of PA in gas phase.<sup>88</sup> The transition state of DHPA formation in aqueous phase is also calculated here to compare the covalent hydration process in gas and bulk aqueous phase (Fig. S13A). A recent *ab initio* metadynamics<sup>105</sup> calculations of explicitly solvated PA showed C<sub>carbonyl</sub> is always interacting with O<sub>water</sub> and that PA spontaneously deprotonates after 5 ps, and the resulting pyruvate anion conforms to a slightly twisted OCCO(H) dihedral angle ( $\sim -92^\circ$ ), which resembles PAHT<sub>a</sub> and PAHT<sub>b</sub> structures. Our IRC calculations in aqueous phase confirmed this behavior and connected the transition state towards DHPA from Tc–H<sub>2</sub>O<sub>b</sub> (Fig. S9A), where H<sub>2</sub>O is positioned parallel to the C<sub>methyl</sub>–C<sub>keto</sub>–C<sub>acid</sub>–O<sub>carboxyl</sub> plane. This is also not the lowest energy Tc-water complex in aqueous phase (Fig. S9A and Table S3A). In DHPA–H<sub>2</sub>O formation in aqueous phase, IRC calculation showed that the transition state is connected to Tc–2H<sub>2</sub>O (Fig. S13A), which is similar in structure to the

starting Tc-dihydrated complex in gas phase<sup>44</sup> where the water molecules are intermolecularly H-bonded to the  $H_{\text{carboxyl}}$  and the doubly-bonded  $O_{\text{carboxyl}}$  below the methyl group.

**Reaction thermodynamics of DHPA and DHPA–H<sub>2</sub>O formation.** The favorability of the complexation process of the starting PA-water complexes dictates the formation of DHPA and DHPA–H<sub>2</sub>O. Both Tc–H<sub>2</sub>O<sub>a</sub> and Tc–2H<sub>2</sub>O complex formations are slightly less favorable than DHPA and DHPA–H<sub>2</sub>O formation in gas phase, respectively, because complexation from individual PA and water molecules involves large entropic lowering compared to covalent hydration, which already starts from these complexes (gas, Table 5). Both complexation and covalent hydration processes in gas phase have negative enthalpies, which means these reactions will be spontaneous at lower temperatures.

In contrast, two scenarios could happen in aqueous phase that might explain why the abundance of DHPA and DHPA–H<sub>2</sub>O in aqueous phase is significantly lower than in a water-restricted environment<sup>55</sup> or, in this calculation, the gas phase. The free energy of Tc–H<sub>2</sub>O<sub>a</sub> complexation in aqueous phase is comparable to the gas phase, which also has a negative enthalpy (aqueous, Table 5). However, conversion of Tc–H<sub>2</sub>O<sub>a</sub> complex to DHPA is comparatively very unfavorable, with positive enthalpy which means even at lower temperatures, the covalent hydration would still be a non-spontaneous reaction. While Tc–2H<sub>2</sub>O conversion to DHPA–H<sub>2</sub>O is slightly more energetically favorable in aqueous phase than gas phase, the complexation of water to Tc–H<sub>2</sub>O<sub>a</sub> is highly unfavorable, with a positive enthalpy.

A previous study reported an indistinguishable abundance between DHPA–H<sub>2</sub>O and DHPA in a water-restricted environment.<sup>55</sup> Although rates of DHPA–H<sub>2</sub>O are slower than DHPA formation in gas phase,<sup>44</sup> there are two possible pathways in forming DHPA–H<sub>2</sub>O compared to

DHPA formation. DHPA–H<sub>2</sub>O can be formed directly from Tc–2H<sub>2</sub>O complex, or H<sub>2</sub>O can attack the newly formed DHPA (Table 5). A more generalized scheme of DHPA and DHPA–H<sub>2</sub>O formation from PA-water complexes is shown in Scheme S1A and S2A, respectively.

**Covalent hydration mechanism of PA in gas and bulk aqueous phase.** Similar to the previous gas phase calculations,<sup>44</sup> additional H<sub>2</sub>O lowers the energy barrier (37.84 kcal/mol) towards DHPA–H<sub>2</sub>O formation from Tc–2H<sub>2</sub>O compared to DHPA formation (41.83 kcal/mol) in aqueous phase, which indicates the cooperative behavior of H<sub>2</sub>O in facilitating covalent hydration of PA (Table 6). The higher formation barriers of DHPA and DHPA–H<sub>2</sub>O in aqueous phase (39.55 and 34.33 kcal/mol, respectively) compared to gas phase<sup>44</sup> can be attributed to the higher energies needed to overcome the solvent stabilization offered by the bulk aqueous potential. In both phases, the TS in DHPA–H<sub>2</sub>O formation is stabilized by the additional H<sub>2</sub>O (Fig. S13A), which disrupts the intramolecular H-bond. The complexed water pulls the electron density away from the carbonyl carbon more efficiently than the intramolecular H-bond offered by the TS of DHPA (Fig. S13A), making the carbonyl carbon more prone to attack by another water towards covalent hydration. This led to an exothermic reaction (Table 6), with DHPA–H<sub>2</sub>O stabilized by a strong lone pair donation of O<sub>water</sub> to the OH<sub>carboxyl</sub> σ\* orbital of DHPA subunit (Table S18B (gas), Table S19B (aqueous)). In comparison, the strongest intramolecular stabilization of the DHPA product is only from a weak σ electron donation of OH<sub>hydroxyl</sub> to π\* orbital of the C=O<sub>carboxyl</sub> (Table S17B), creating a less energetically favorable product in gas and even leading to an endothermic process in aqueous phase (Table 6), also due to a less stable reactant (Tc–H<sub>2</sub>O<sub>b</sub>).

**Rates of DHPA and DHPA–H<sub>2</sub>O.** The  $E_a$  of DHPA formation in aqueous phase, calculated from both *ab initio* (Table 6) and TST methods (Table S2A), is higher than in the gas phase. Hence it has a slower rate at lower temperatures compared to the gas phase (Fig. 6). On the other hand, even with a higher  $E_a$  in aqueous phase, DHPA–H<sub>2</sub>O formation in the aqueous phase has higher temperature dependence ( $n$ ) in its pre-exponential factor compared to gas phase (2.50 vs. 1.32, Table S2A). This means the rate increases more as temperature increases, and thus the rate of DHPA–H<sub>2</sub>O is faster in aqueous phase than in the gas phase (Fig. 6). Both gas and aqueous phase  $E_a$  of DHPA formation are higher than DHPA–H<sub>2</sub>O. However, the pre-exponential factors of both processes in aqueous phase are very similar (parameters using TST with Eckart tunneling, Table S2A), unlike the gas phase (Fig. 6), DHPA–H<sub>2</sub>O formation competes with DHPA formation in aqueous phase. It is important to note that DHPA formation in aqueous phase is an endothermic process, in contrast to the gas phase, and starts from a different stable Tc monohydrate (Tc–H<sub>2</sub>O<sub>b</sub>). This means the reverse reaction is more likely to happen, contributing to a slower than expected rate.

#### 4 Conclusions

The role of both intramolecular and intermolecular H-bonding on PA degradation, conformational switching, complexation, and hydration has been characterized in this study. The strength of intramolecular H-bonding of Tc conformer in aqueous phase is weakened due to preferential bulk solvation of carboxylic hydrogen and ketonic oxygen. This slows the H-transfer process, leading to MHC–CO<sub>2</sub> formation. Mechanistically, the bulk solvation also splits the concerted H-transfer and C–C bond cleavage of the MHC formation by stabilizing a new intermediate between these two processes. This new intermediate, PAHT<sub>c</sub>, is only found in

aqueous phase and is stabilized by a strong intramolecular H-bonding between the newly formed alcoholic hydrogen and carboxylate oxygen. The overall effect of bulk solvation changed the degradation mechanism of PA compared to gas phase, which led to slower rates and product branching ratios strongly favoring acetaldehyde but made acetic acid dominate in some conditions. The mechanism shown here supports experimental observation of a lower photolysis rate in aqueous phase<sup>46</sup> and dominance of acetic acid in low energy photolytic experiments in bulk water.<sup>47</sup>

PA's conformational switching is also greatly affected by the strength of intramolecular and intermolecular H-bonding with water. The weakening of Tc's intramolecular H-bonding in aqueous phase reordered the relative energies and abundance of the conformers. H-bond strength directly correlates to the type of orbital interaction. Intramolecular H-bonds containing  $p$  to  $\sigma^*$  interaction (Tc) is much stronger than  $\sigma$  to  $\pi^*$  interaction (Tt and Ct). However, the  $p$  to  $\sigma^*$  interaction is significantly weakened by bulk solvation compared  $\sigma$  to  $\pi^*$  interaction. This supports previous experimental studies in aqueous phase where Tt conformer's distribution increased or even surpassed Tc.<sup>46</sup> For PA-water complexes, the stabilization of PA's carboxylic hydrogen is the main driving force of the energy lowering of the complexes in both gas and aqueous phase. NBO characterized the lowest energy complexes to be stabilized by a strong (primary) intermolecular H-bond which always involves electron donation of the  $p$  orbital  $O_{\text{water}}$  molecule to the  $\sigma^*$  orbital of the  $\text{OH}_{\text{carboxyl}}$  of PA. In general, less charge differences of the H-bonded atoms are observed for the stronger type of H-bonding upon solvation. This behavior indicates aggressive competition between H-bonding and bulk solvation in stabilizing polar regions. The lowest energy PA-water complexes also have OH-O bond angles of the

intermolecular H-bonds closer to  $180^\circ$  and have the greatest  $\Delta$ distance upon solvation, which signifies more efficient orbital overlap. Secondary orbital interactions are also seen to support the stabilization of these complexes. Although these interactions are of  $\rho$  to  $\sigma^*$  type of intermolecular H-bonding, electron donation from doubly-bonded oxygen atoms of PA to OH group of water is always significantly weaker than the primary intermolecular H-bond.

In PA's hydration, it has been shown that the H-bonded PA-water complexes are indeed the precursors for PA's covalently hydrated forms, DHPA and DHPA-H<sub>2</sub>O, in both gas<sup>44</sup> and aqueous phase, corroborating with the previous claims.<sup>55</sup> In both phases, the cooperative behavior of H<sub>2</sub>O is seen in the lowering of barriers for the formation of DHPA-H<sub>2</sub>O than DHPA. The TS in DHPA-H<sub>2</sub>O formation is stabilized by the additional H<sub>2</sub>O, disrupting the intramolecular H-bond and pulling the electron density away from the carbonyl carbon more efficiently than the intramolecular H-bond offered by the TS of DHPA, making it more prone to a water attack. The thermodynamics of PA-water complexation, DHPA, and DHPA-H<sub>2</sub>O formation also shows favorable complexation in gas phase compared to aqueous phase, supporting previous work of the abundance of DHPA in a water-restricted environment.<sup>55</sup>

**Implications.** The concentration of water in the troposphere varies in different environments and altitudes. More water can be found in the lower atmosphere, especially near the ocean surface, and concentration decreases as we go higher. As reported in this study, the characteristics of PA's conformational switching, thermal decomposition, complexation, and covalent hydration in gas and aqueous environments are very different due to the dependency of H-bonding behavior on water concentration. PA is a vital part of atmospheric keto-acid

chemistry; thus, changes in these characteristics will affect aerosol formation in a different environment.

### **Author contributions**

MDPB and MLM designed the study, performed the calculations, and interpreted the data. MDPB and MLM contributed to the writing and reviewing of the final version of this article.

### **Conflicts of interest**

There are no conflicts to declare.

### **Acknowledgements**

This research was supported by UMass Dartmouth's faculty research start-up and the Seed Funding program from the Office of the Provost. This research used the computing resources of UMass Dartmouth and the University of Massachusetts Green High-Performance Computing Cluster. MDPB gratefully acknowledged the summer funding from the Center for Scientific Computing and Data Science Research of UMass Dartmouth. The authors also acknowledged the support from ONR DURIP Grant No. N00014-18-1-2255.

### **Notes and references**

‡ Electronic supplementary information (ESI) available: Supplementary A contains structures of lactone isomers, PAHT monomers, water complexes of PA, PAHT, and DHPA, transition states and minima along PA PES and DHPA formation in aqueous phase; temporal dependence at 500 fs and exit channel ratio; plot of the effect of pressure on RRKM rates; calculated parameters of the least-square fit of the Arrhenius plots; and thermodynamic properties of PA complexes in

gas and aqueous phase. Supplementary B and C contains selected NBO analyses and optimized coordinates, respectively.

- 1 S. Liu, D. A. Day, J. E. Shields and L. M. Russell, Ozone-driven daytime formation of secondary organic aerosol containing carboxylic acid groups and alkane groups, *Atmospheric Chem. Phys.*, 2011, **11**, 8321–8341.
- 2 V.-M. Kerminen, X. Chen, V. Vakkari, T. Petäjä, M. Kulmala and F. Bianchi, Atmospheric new particle formation and growth: review of field observations, *Environ. Res. Lett.*, 2018, **13**, 103003.
- 3 F. Yu, Binary  $\text{H}_2\text{SO}_4\text{-H}_2\text{O}$  homogeneous nucleation based on kinetic quasi-unary nucleation model: Look-up tables, *J. Geophys. Res.*, 2006, **111**, D04201.
- 4 I. Napari, M. Noppel, H. Vehkamäki and M. Kulmala, Parametrization of ternary nucleation rates for  $\text{H}_2\text{SO}_4\text{-NH}_3\text{-H}_2\text{O}$  vapors, *J. Geophys. Res. Atmospheres*, 2002, **107**, AAC 6-1-AAC 6-6.
- 5 H. Zhao, S. Tang, X. Xu and L. Du, Hydrogen Bonding Interaction between Atmospheric Gaseous Amides and Methanol, *Int. J. Mol. Sci.*, 2017, **18**, 4.
- 6 M. C. Facchini, M. Mircea, S. Fuzzi and R. J. Charlson, Cloud albedo enhancement by surface-active organic solutes in growing droplets, *Nature*, 1999, **401**, 257–259.
- 7 K. T. Malecha and S. A. Nizkorodov, Photodegradation of Secondary Organic Aerosol Particles as a Source of Small, Oxygenated Volatile Organic Compounds, *Environ. Sci. Technol.*, 2016, **50**, 9990–9997.
- 8 H. K. Maben and P. J. Ziemann, Kinetics of oligomer-forming reactions involving the major functional groups present in atmospheric secondary organic aerosol particles, *Environ. Sci. Process. Impacts*, 2022, 10.1039.D2EM00124A.
- 9 B. Ervens, A modeling study of aqueous production of dicarboxylic acids: 1. Chemical pathways and speciated organic mass production, *J. Geophys. Res.*, 2004, **109**, D15205.
- 10 D. A. Amaladhasan, C. Heyn, C. R. Hoyle, I. El Haddad, M. Elser, S. M. Pieber, J. G. Slowik, A. Amorim, J. Duplissy, S. Ehrhart, V. Makhmutov, U. Molteni, M. Rissanen, Y. Stozhkov, R. Wagner, A. Hansel, J. Kirkby, N. M. Donahue, R. Volkamer, U. Baltensperger, M. Gysel-Beer and A. Zuend, Modelling the gas–particle partitioning and water uptake of isoprene-derived secondary organic aerosol at high and low relative humidity, *Atmospheric Chem. Phys.*, 2022, **22**, 215–244.
- 11 Y. B. Lim, Y. Tan and B. J. Turpin, Chemical insights, explicit chemistry, and yields of secondary organic aerosol from OH radical oxidation of methylglyoxal and glyoxal in the aqueous phase, *Atmospheric Chem. Phys.*, 2013, **13**, 8651–8667.
- 12 A. E. Reed Harris, A. Pajunoja, M. Cazaunau, A. Gratien, E. Pangui, A. Monod, E. C. Griffith, A. Virtanen, J.-F. Doussin and V. Vaida, Multiphase Photochemistry of Pyruvic Acid under Atmospheric Conditions, *J. Phys. Chem. A*, 2017, **121**, 3327–3339.
- 13 Y. Fu, Y. Zhang, F. Zhang, J. Chen, Z. Zhu and X.-Y. Yu, Does interfacial photochemistry play a role in the photolysis of pyruvic acid in water?, *Atmos. Environ.*, 2018, **191**, 36–45.
- 14 J. G. Pruyne, M.-T. Lee, C. Fábri, A. Beloqui Redondo, A. Kleibert, M. Ammann, M. A. Brown and M. J. Krisch, Liquid–Vapor Interface of Formic Acid Solutions in Salt Water: A Comparison of Macroscopic Surface Tension and Microscopic in Situ X-ray Photoelectron Spectroscopy Measurements, *J. Phys. Chem. C*, 2014, **118**, 29350–29360.
- 15 P. B. Petersen and R. J. Saykally, On the Nature of Ions at the Liquid Water Surface, *Annu. Rev. Phys. Chem.*, 2006, **57**, 333–364.
- 16 R. Ciuraru, L. Fine, M. van Pinxteren, B. D’Anna, H. Herrmann and C. George, Photosensitized production of functionalized and unsaturated organic compounds at the air-sea interface, *Sci. Rep.*, 2015, **5**, 12741.

- 17 M. Brüggemann, N. Hayeck, C. Bonnineau, S. Pesce, P. A. Alpert, S. Perrier, C. Zuth, T. Hoffmann, J. Chen and C. George, Interfacial photochemistry of biogenic surfactants: a major source of abiotic volatile organic compounds, *Faraday Discuss.*, 2017, **200**, 59–74.
- 18 M. O. Andreae, R. W. Talbot and S.-M. Li, Atmospheric measurements of pyruvic and formic acid, *J. Geophys. Res. Atmospheres*, 1987, **92**, 6635–6641.
- 19 R. W. Talbot, M. O. Andreae, H. Berresheim, D. J. Jacob and K. M. Beecher, Sources and sinks of formic, acetic, and pyruvic acids over central Amazonia: 2. Wet season, *J. Geophys. Res. Atmospheres*, 1990, **95**, 16799–16811.
- 20 K. E. Altieri, A. G. Carlton, H.-J. Lim, B. J. Turpin and S. P. Seitzinger, Evidence for Oligomer Formation in Clouds: Reactions of Isoprene Oxidation Products, *Environ. Sci. Technol.*, 2006, **40**, 4956–4960.
- 21 K. Kawamura, H. Kasukabe and L. A. Barrie, Secondary formation of water-soluble organic acids and  $\alpha$ -dicarbonyls and their contributions to total carbon and water-soluble organic carbon: Photochemical aging of organic aerosols in the Arctic spring, *J. Geophys. Res.*, 2010, **115**, D21306.
- 22 B. Ervens, A. G. Carlton, B. J. Turpin, K. E. Altieri, S. M. Kreidenweis and G. Feingold, Secondary organic aerosol yields from cloud-processing of isoprene oxidation products, *Geophys. Res. Lett.*, 2008, **35**, L02816.
- 23 K. F. Ho, S. C. Lee, J. J. Cao, K. Kawamura, T. Watanabe, Y. Cheng and J. C. Chow, Dicarboxylic acids, ketocarboxylic acids and dicarbonyls in the urban roadside area of Hong Kong, *Atmos. Environ.*, 2006, **40**, 3030–3040.
- 24 P. Veres, J. M. Roberts, I. R. Burling, C. Warneke, J. de Gouw and R. J. Yokelson, Measurements of gas-phase inorganic and organic acids from biomass fires by negative-ion proton-transfer chemical-ionization mass spectrometry, *J. Geophys. Res.*, 2010, **115**, D23302.
- 25 P. G. Eger, J. Schuladen, N. Sobanski, H. Fischer, E. Karu, J. Williams, M. Riva, Q. Zha, M. Ehn, L. L. J. Quéléver, S. Schallhart, J. Lelieveld and J. N. Crowley, Pyruvic acid in the boreal forest: gas-phase mixing ratios and impact on radical chemistry, *Atmospheric Chem. Phys.*, 2020, **20**, 3697–3711.
- 26 M. Shiraiwa, A. Zuend, A. K. Bertram and J. H. Seinfeld, Gas–particle partitioning of atmospheric aerosols: interplay of physical state, non-ideal mixing and morphology, *Phys. Chem. Chem. Phys.*, 2013, **15**, 11441–11453.
- 27 M. Md. M. Hoque, K. Kawamura and M. Uematsu, Spatio-temporal distributions of dicarboxylic acids,  $\omega$ -oxocarboxylic acids, pyruvic acid,  $\alpha$ -dicarbonyls and fatty acids in the marine aerosols from the North and South Pacific, *Atmospheric Res.*, 2017, **185**, 158–168.
- 28 M. M. M. Hoque and K. Kawamura, Longitudinal distributions of dicarboxylic acids,  $\omega$ -oxoacids, pyruvic acid,  $\alpha$ -dicarbonyls, and fatty acids in the marine aerosols from the central Pacific including equatorial upwelling, *Glob. Biogeochem. Cycles*, 2016, **30**, 534–548.
- 29 P. Warneck, Multi-Phase Chemistry of C2 and C3 Organic Compounds in the Marine Atmosphere, *J. Atmospheric Chem.*, 2005, **51**, 119–159.
- 30 R. Sempéré and K. Kawamura, Comparative distributions of dicarboxylic acids and related polar compounds in snow, rain and aerosols from urban atmosphere, *Atmos. Environ.*, 1994, **28**, 449–459.
- 31 M. I. Guzmán, M. R. Hoffmann and A. J. Colussi, Photolysis of pyruvic acid in ice: Possible relevance to CO and CO<sub>2</sub> ice core record anomalies, *J. Geophys. Res. Atmospheres*, 2007, **112**, D10123.
- 32 M. I. Guzmán, L. Hildebrandt, A. J. Colussi and M. R. Hoffmann, Cooperative Hydration of Pyruvic Acid in Ice, *J. Am. Chem. Soc.*, 2006, **128**, 10621–10624.
- 33 S. Yamamoto and R. A. Back, The photolysis and thermal decomposition of pyruvic acid in the gas phase, *Can. J. Chem.*, 1985, **63**, 549–554.
- 34 R. Taylor, The mechanism of thermal eliminations part XXIII: [1] The thermal decomposition of pyruvic acid, *Int. J. Chem. Kinet.*, 1987, **19**, 709–713.
- 35 K. Saito, G. Sasaki, K. Okada and S. Tanaka, Unimolecular Decomposition of Pyruvic Acid: An Experimental and Theoretical Study, *J. Phys. Chem.*, 1994, **98**, 3756–3761.

- 36 R. N. Rosenfeld and B. Weiner, Energy disposal in the photofragmentation of pyruvic acid in the gas phase, *J. Am. Chem. Soc.*, 1983, **105**, 3485–3488.
- 37 D. Grosjean, Atmospheric reactions of pyruvic acid, *Atmospheric Environ. 1967*, 1983, **17**, 2379–2382.
- 38 A. E. Reed Harris, J.-F. Doussin, B. K. Carpenter and V. Vaida, Gas-Phase Photolysis of Pyruvic Acid: The Effect of Pressure on Reaction Rates and Products, *J. Phys. Chem. A*, 2016, **120**, 10123–10133.
- 39 M. G. M. Berges and P. Warneck, Product Quantum Yields for the 350 nm Photodecomposition of Pyruvic Acid in Air, *Berichte Bunsenges. Für Phys. Chem.*, 1992, **96**, 413–416.
- 40 A. E. Reed Harris, M. Cazaunau, A. Gratien, E. Pangui, J.-F. Doussin and V. Vaida, Atmospheric Simulation Chamber Studies of the Gas-Phase Photolysis of Pyruvic Acid, *J. Phys. Chem. A*, 2017, **121**, 8348–8358.
- 41 A. Mellouki and Y. Mu, On the atmospheric degradation of pyruvic acid in the gas phase, *J. Photochem. Photobiol. Chem.*, 2003, **157**, 295–300.
- 42 P. R. Schreiner, H. P. Reisenauer, D. Ley, D. Gerbig, C.-H. Wu and W. D. Allen, Methylhydroxycarbene: Tunneling Control of a Chemical Reaction, *Science*, 2011, **332**, 1300–1303.
- 43 B. R. Samanta, R. Fernando, D. Rösch, H. Reisler and D. L. Osborn, Primary photodissociation mechanisms of pyruvic acid on S1: observation of methylhydroxycarbene and its chemical reaction in the gas phase, *Phys Chem Chem Phys*, 2021, **23**, 4107–4119.
- 44 M. D. P. Barquilla and M. L. Mayes, A computational study of the gas-phase pyruvic acid decomposition: Potential energy surfaces, temporal dependence, and rates, *AIP Adv.*, 2021, **11**, 015243.
- 45 K. Takahashi, K. L. Plath, R. T. Skodje and V. Vaida, Dynamics of Vibrational Overtone Excited Pyruvic Acid in the Gas Phase: Line Broadening through Hydrogen-Atom Chattering, *J. Phys. Chem. A*, 2008, **112**, 7321–7331.
- 46 S. L. Blair, A. E. Reed Harris, B. N. Frandsen, H. G. Kjaergaard, E. Pangui, M. Cazaunau, J.-F. Doussin and V. Vaida, Conformer-Specific Photolysis of Pyruvic Acid and the Effect of Water, *J. Phys. Chem. A*, 2020, **124**, 1240–1252.
- 47 A. E. Reed Harris, B. Ervens, R. K. Shoemaker, J. A. Kroll, R. J. Rapf, E. C. Griffith, A. Monod and V. Vaida, Photochemical Kinetics of Pyruvic Acid in Aqueous Solution, *J. Phys. Chem. A*, 2014, **118**, 8505–8516.
- 48 K. J. Kappes, A. M. Deal, M. F. Jaspersen, S. L. Blair, J.-F. Doussin, M. Cazaunau, E. Pangui, B. N. Hopper, M. S. Johnson and V. Vaida, Chemistry and Photochemistry of Pyruvic Acid at the Air–Water Interface, *J. Phys. Chem. A*, 2021, **125**, 1036–1049.
- 49 M. I. Guzmán, A. J. Colussi and M. R. Hoffmann, Photogeneration of Distant Radical Pairs in Aqueous Pyruvic Acid Glasses, *J. Phys. Chem. A*, 2006, **110**, 931–935.
- 50 M. I. Guzmán, A. J. Colussi and M. R. Hoffmann, Photoinduced Oligomerization of Aqueous Pyruvic Acid, *J. Phys. Chem. A*, 2006, **110**, 3619–3626.
- 51 R. J. Rapf, R. J. Perkins, B. K. Carpenter and V. Vaida, Mechanistic Description of Photochemical Oligomer Formation from Aqueous Pyruvic Acid, *J. Phys. Chem. A*, 2017, **121**, 4272–4282.
- 52 E. C. Griffith, B. K. Carpenter, R. K. Shoemaker and V. Vaida, Photochemistry of aqueous pyruvic acid, *Proc. Natl. Acad. Sci.*, 2013, **110**, 11714–11719.
- 53 R. J. Rapf, M. R. Dooley, K. Kappes, R. J. Perkins and V. Vaida, pH Dependence of the Aqueous Photochemistry of  $\alpha$ -Keto Acids, *J. Phys. Chem. A*, 2017, **121**, 8368–8379.
- 54 D. Shemesh, M. Luo, V. H. Grassian and R. B. Gerber, Absorption spectra of pyruvic acid in water: insights from calculations for small hydrates and comparison to experiment, *Phys. Chem. Chem. Phys.*, 2020, **22**, 12658–12670.

- 55 M. K. Maroń, K. Takahashi, R. K. Shoemaker and V. Vaida, Hydration of pyruvic acid to its geminal-diol, 2,2-dihydroxypropanoic acid, in a water-restricted environment, *Chem. Phys. Lett.*, 2011, **513**, 184–190.
- 56 Y. Pocker, J. E. Meany, B. J. Nist and C. Zadorojny, Reversible hydration of pyruvic acid. I. Equilibrium studies, *J. Phys. Chem.*, 1969, **73**, 2879–2882.
- 57 H.-J. Buschmann, H.-H. Földner and W. Knoche, The Reversible Hydration of Carbonyl Compounds in Aqueous Solution. Part I, The Keto/Gem-diol Equilibrium, *Berichte Bunsenges. Für Phys. Chem.*, 1980, **84**, 41–44.
- 58 M. Luo, D. Shemesh, M. N. Sullivan, M. R. Alves, M. Song, R. B. Gerber and V. H. Grassian, Impact of pH and NaCl and CaCl<sub>2</sub> Salts on the Speciation and Photochemistry of Pyruvic Acid in the Aqueous Phase, *J. Phys. Chem. A*, 2020, **124**, 5071–5080.
- 59 Z. Zhang, L. Liu, C. Liu and W. Cai, Studies on the sea surface microlayer. II. The layer of sudden change of physical and chemical properties, *J. Colloid Interface Sci.*, 2003, **264**, 148–159.
- 60 Z. Zhang, W. Cai, L. Liu, C. Liu and F. Chen, Direct determination of thickness of sea surface microlayer using a pH microelectrode at original location, *Sci. China Ser. B Chem.*, 2003, **46**, 339–351.
- 61 R. L. Craig, L. Nandy, J. L. Axson, C. S. Dutcher and A. P. Ault, Spectroscopic Determination of Aerosol pH from Acid–Base Equilibria in Inorganic, Organic, and Mixed Systems, *J. Phys. Chem. A*, 2017, **121**, 5690–5699.
- 62 A. Bougiatioti, P. Nikolaou, I. Stavroulas, G. Kouvarakis, R. Weber, A. Nenes, M. Kanakidou and N. Mihalopoulos, Particle water and pH in the eastern Mediterranean: source variability and implications for nutrient availability, *Atmospheric Chem. Phys.*, 2016, **16**, 4579–4591.
- 63 R. J. Weber, H. Guo, A. G. Russell and A. Nenes, High aerosol acidity despite declining atmospheric sulfate concentrations over the past 15 years, *Nat. Geosci.*, 2016, **9**, 282–285.
- 64 A. H. Young, W. C. Keene, A. A. P. Pszenny, R. Sander, J. A. Thornton, T. P. Riedel and J. R. Maben, Phase partitioning of soluble trace gases with size-resolved aerosols in near-surface continental air over northern Colorado, USA, during winter, *J. Geophys. Res. Atmospheres*, 2013, **118**, 9414–9427.
- 65 J. G. Murphy, P. K. Gregoire, A. G. Tevlin, G. R. Wentworth, R. A. Ellis, M. Z. Markovic and T. C. VandenBoer, Observational constraints on particle acidity using measurements and modelling of particles and gases, *Faraday Discuss.*, 2017, **200**, 379–395.
- 66 H. Guo, L. Xu, A. Bougiatioti, K. M. Cerully, S. L. Capps, J. R. J. Hite, A. G. Carlton, S.-H. Lee, M. H. Bergin, N. L. Ng, A. Nenes and R. J. Weber, Fine-particle water and pH in the southeastern United States, *Atmospheric Chem. Phys.*, 2015, **15**, 5211–5228.
- 67 A. J. Eugene, E. A. Pillar, A. J. Colussi and M. I. Guzman, Enhanced Acidity of Acetic and Pyruvic Acids on the Surface of Water, *Langmuir*, 2018, **34**, 9307–9313.
- 68 E. C. Griffith, A. F. Tuck and V. Vaida, Ocean–Atmosphere Interactions in the Emergence of Complexity in Simple Chemical Systems, *Acc. Chem. Res.*, 2012, **45**, 2106–2113.
- 69 C. M. Dobson, G. B. Ellison, A. F. Tuck and V. Vaida, Atmospheric aerosols as prebiotic chemical reactors, *Proc. Natl. Acad. Sci.*, 2000, **97**, 11864–11868.
- 70 P. A. Sigala, E. A. Ruben, C. W. Liu, P. M. B. Piccoli, E. G. Hohenstein, T. J. Martínez, A. J. Schultz and D. Herschlag, Determination of Hydrogen Bond Structure in Water versus Aprotic Environments To Test the Relationship Between Length and Stability, *J. Am. Chem. Soc.*, 2015, **137**, 5730–5740.
- 71 S. Grimme, S. Ehrlich and L. Goerigk, Effect of the damping function in dispersion corrected density functional theory, *J. Comput. Chem.*, 2011, **32**, 1456–1465.
- 72 S. Grimme, J. Antony, S. Ehrlich and H. Krieg, A consistent and accurate ab initio parametrization of density functional dispersion correction (DFT-D) for the 94 elements H–Pu, *J. Chem. Phys.*, 2010, **132**, 154104.

- 73 R. A. Kendall, T. H. Dunning and R. J. Harrison, Electron affinities of the first-row atoms revisited. Systematic basis sets and wave functions, *J. Chem. Phys.*, 1992, **96**, 6796–6806.
- 74 A. V. Marenich, C. J. Cramer and D. G. Truhlar, Universal Solvation Model Based on Solute Electron Density and on a Continuum Model of the Solvent Defined by the Bulk Dielectric Constant and Atomic Surface Tensions, *J. Phys. Chem. B*, 2009, **113**, 6378–6396.
- 75 T. B. Adler, G. Knizia and H.-J. Werner, A simple and efficient CCSD(T)-F12 approximation, *J. Chem. Phys.*, 2007, **127**, 221106.
- 76 N. Sylvetsky, M. K. Kesharwani and J. M. L. Martin, The aug-cc-pVnZ-F12 basis set family: Correlation consistent basis sets for explicitly correlated benchmark calculations on anions and noncovalent complexes, *J. Chem. Phys.*, 2017, **147**, 134106.
- 77 . D. Glendening, J. K. Badenhoop, A. E. Reed, J. E. Carpenter, J. A. Bohmann, C. M. Morales, C. R. Landis, and F. Weinhold, NATURAL BOND ORBITAL 6.0, Theoretical Chemistry Institute, University of Wisconsin, Madison, WI, 2013.
- 78 F. Neese, The ORCA program system: The ORCA program system, *Wiley Interdiscip. Rev. Comput. Mol. Sci.*, 2012, **2**, 73–78.
- 79 T. Beyer and D. F. Swinehart, Algorithm 448: Number of Multiply-restricted Partitions, *Commun ACM*, 1973, **16**, 379-.
- 80 A. C. Mansell, D. J. Kahle and D. J. Bellert, Calculating RRKM Rate Constants from Vibrational Frequencies and Their Dynamic Interpretation, *Math. J.*, 2017, **19**, 1–20.
- 81 Wolfram Research, Inc., Mathematica, Version 12.0, Champaign, IL (2019).
- 82 S. Canneaux, F. Bohr and E. Henon, KiSThEP: A program to predict thermodynamic properties and rate constants from quantum chemistry results<sup>†</sup>, *J. Comput. Chem.*, 2014, **35**, 82–93.
- 83 J. H. Olson, The properties of gases and liquids: Their estimation and correlation, Robert C. Reid and Thomas K. Sherwood, McGraw-Hill Book Company, Inc., New York (1958). 386 pages. \$10.00., *AIChE J.*, 1958, **4**, 500–10D.
- 84 K. G. Joback and R. C. Reid, Estimation of Pure-Component Properties from Group-Contributions, *Chem. Eng. Commun.*, 1987, **57**, 233–243.
- 85 F. M. Mourits and F. H. A. Rummens, A critical evaluation of Lennard–Jones and Stockmayer potential parameters and of some correlation methods, *Can. J. Chem.*, 1977, **55**, 3007–3020.
- 86 R. Kakkar, M. Pathak and P. Gahlot, Effect of aqueous solvation on the structures of pyruvic acid isomers and their reactions in solution: a computational study, *J. Phys. Org. Chem.*, 2008, **21**, 23–29.
- 87 E. G. Schnitzler, N. A. Seifert, S. Ghosh, J. Thomas, Y. Xu and W. Jäger, Hydration of the simplest  $\alpha$ -keto acid: a rotational spectroscopic and ab initio study of the pyruvic acid–water complex, *Phys. Chem. Chem. Phys.*, 2017, **19**, 4440–4446.
- 88 F. Hammami and N. Issaoui, A DFT Study of the Hydrogen Bonded Structures of Pyruvic Acid–Water Complexes, *Front. Phys.*, 2022, **10**, 1–9.
- 89 C. J. Cramer and D. G. Truhlar, AM1-SM2 and PM3-SM3 parameterized SCF solvation models for free energies in aqueous solution, *J. Comput. Aided Mol. Des.*, 1992, **6**, 629–666.
- 90 P. I. Nagy, Competing Intramolecular vs. Intermolecular Hydrogen Bonds in Solution, *Int. J. Mol. Sci.*, 2014, **15**, 19562–19633.
- 91 G. da Silva, Decomposition of Pyruvic Acid on the Ground-State Potential Energy Surface, *J. Phys. Chem. A*, 2016, **120**, 276–283.
- 92 X.-P. Chang, Q. Fang and G. Cui, Mechanistic photodecarboxylation of pyruvic acid: Excited-state proton transfer and three-state intersection, *J. Chem. Phys.*, 2014, **141**, 154311.
- 93 K. E. Norris and J. E. Gready, Mechanistic aspects of biological redox reactions involving NADH. Part 4. Possible mechanisms and corresponding intermediates for the catalytic reaction in L-lactate dehydrogenase, *J. Mol. Struct. THEOCHEM*, 1993, **279**, 99–125.
- 94 G. A. Brooks, Intra- and extra-cellular lactate shuttles, *Med. Sci. Sports Exerc.*, 2000, **32**, 790–799.

- 95 A. Schurr, Lactate: the ultimate cerebral oxidative energy substrate?, *J. Cereb. Blood Flow Metab. Off. J. Int. Soc. Cereb. Blood Flow Metab.*, 2006, **26**, 142–152.
- 96 M. J. Rogatzki, B. S. Ferguson, M. L. Goodwin and L. B. Gladden, Lactate is always the end product of glycolysis, *Front. Neurosci.*, 2015, **9**, 1–7.
- 97 A. A. Schurr, in *Carbohydrate*, ed. M. Caliskan, I. H. Kavakli, G. C. Oz, IntechOpen, London, 2017, Lactate, Not Pyruvate, Is the End Product of Glucose Metabolism via Glycolysis, 53367.
- 98 H.-H. Carstensen and A. M. Dean, in *Comprehensive Chemical Kinetics*, ed. R. W. Carr, Elsevier, 2007, vol. 42, pp. 101–184.
- 99 C. L. Perrin, Symmetries of Hydrogen Bonds in Solution, *Science*, 1994, **266**, 1665–1668.
- 100 J. A. Gerlt, M. M. Kreevoy, W. Cleland and P. A. Frey, Understanding enzymic catalysis: the importance of short, strong hydrogen bonds, *Chem. Biol.*, 1997, **4**, 259–267.
- 101 W. W. Cleland and M. M. Kreevoy, Low-barrier hydrogen bonds and enzymic catalysis, *Science*, 1994, **264**, 1887–1890.
- 102 Neil. Stahl and W. P. Jencks, Hydrogen bonding between solutes in aqueous solution, *J. Am. Chem. Soc.*, 1986, **108**, 4196–4205.
- 103 H. Pašalić, A. J. A. Aquino, D. Tunega, G. Haberhauer, M. H. Gerzabek, H. C. Georg, T. F. Moraes, K. Coutinho, S. Canuto and H. Lischka, Thermodynamic stability of hydrogen-bonded systems in polar and nonpolar environments, *J. Comput. Chem.*, 2010, **31**, 2046–2055.
- 104 H. Pašalić, D. Tunega, A. J. A. Aquino, G. Haberhauer, M. H. Gerzabek and H. Lischka, The stability of the acetic acid dimer in microhydrated environments and in aqueous solution, *Phys. Chem. Chem. Phys.*, 2012, **14**, 4162–4170.
- 105 R. Pollet and W. Chin, Reversible Hydration of  $\alpha$ -Dicarbonyl Compounds from Ab Initio Metadynamics Simulations: Comparison between Pyruvic and Glyoxylic Acids in Aqueous Solutions, *J. Phys. Chem. B*, 2021, **125**, 2942–2951.

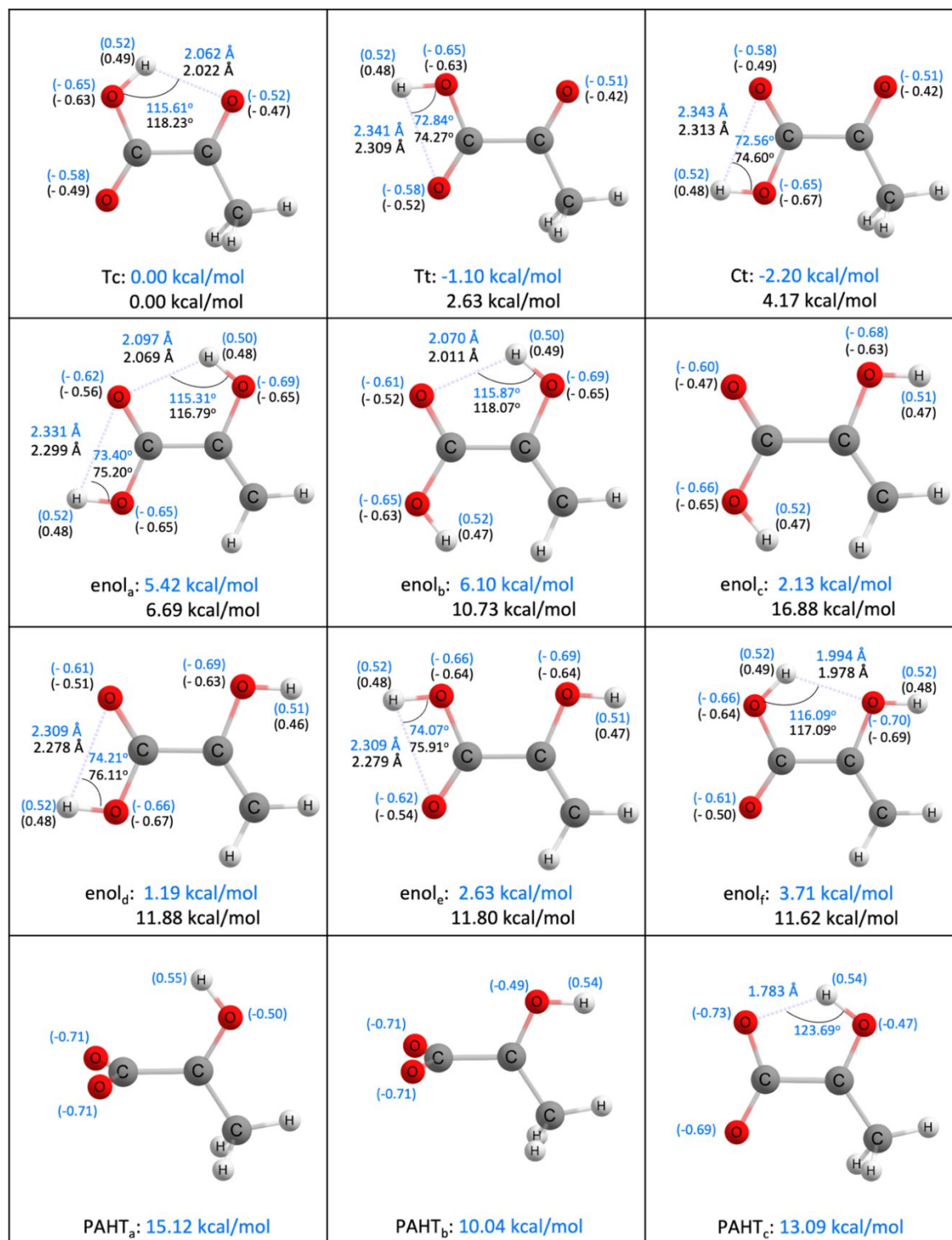
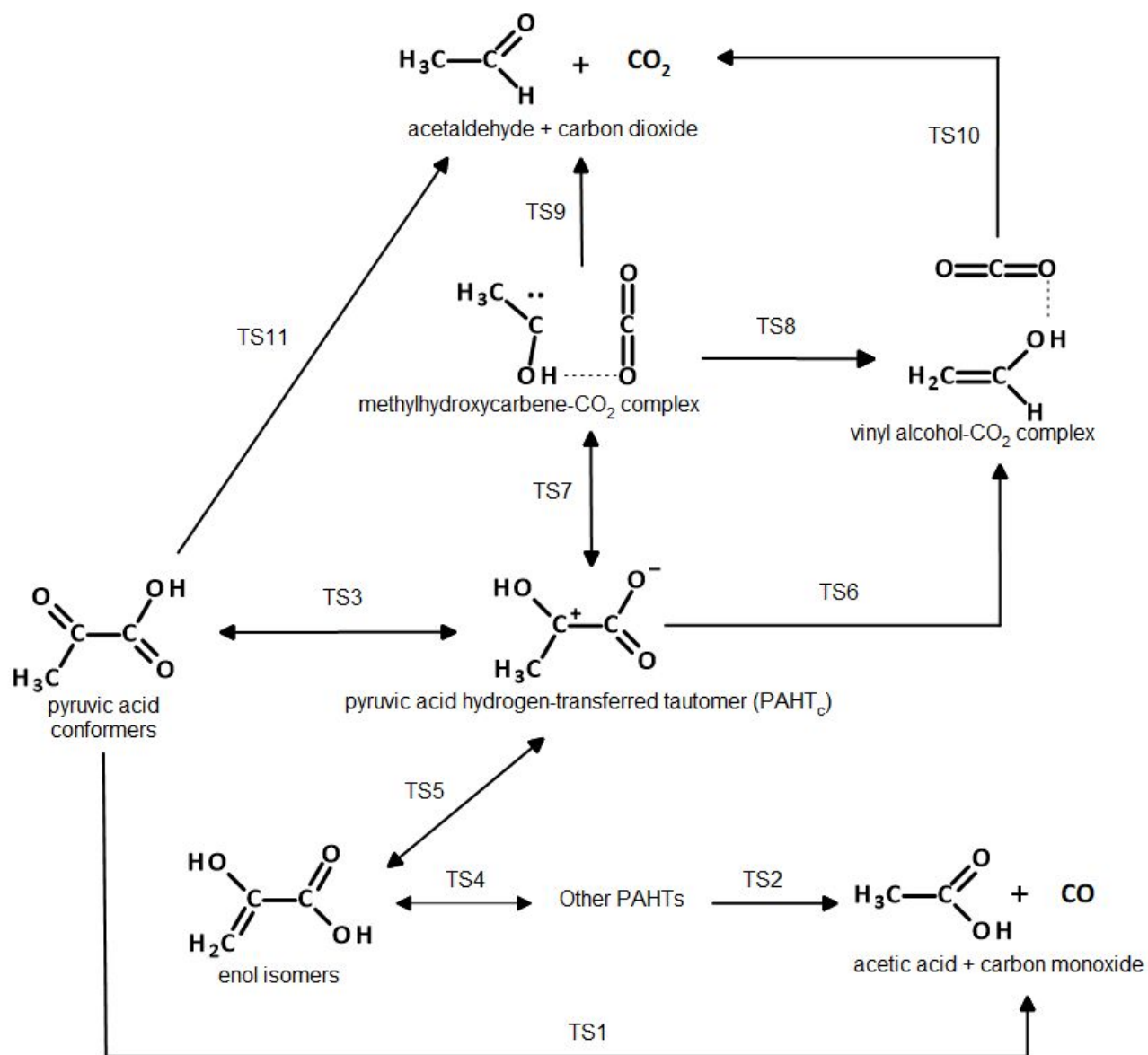


**Fig. 1** Intramolecular H-bond lengths, natural atomic charges (values in parentheses), OH-O bond angles, and relative enthalpies (at 0 K) of pyruvic acid (PA) conformers (Tc, Tt, and Ct), enol isomers, and PA hydrogen-transferred (PAHT) tautomers in aqueous phase (blue), calculated at CCSD(T)-F12/aug-cc-pVDZ-F12//B2PLYP-D3BJ/aug-cc-pVTZ level of theory. SMD was used for the aqueous phase calculations. Gas phase values (black) are taken from previous calculations.<sup>44</sup>

**Table 1** Dominant OH-O orbital interactions of pyruvic acid (PA) conformers and isomers (Fig. 1), calculated by NBO at B2PLYP-D3BJ/aug-cc-pVTZ level of theory. SMD was used for the aqueous phase calculations.

Conformer	Phase	Electron Donor			Electron Acceptor			Type of orbital interaction	Stabilization energy, kcal/mol
		Functional group	Variant	Atom/s	Functional group	Variant	Atom/s		
Tc	gas	carbonyl	lone pair	O	carboxyl	$\sigma$ antibond	O-H	$p$ to $\sigma^*$	3.29
	aqueous	carbonyl	lone pair	O	carboxyl	$\sigma$ antibond	O-H	$p$ to $\sigma^*$	2.45
Tt	gas	carboxyl	$\sigma$ bond	O-H	carboxyl	$\pi$ antibond	C=O	$\sigma$ to $\pi^*$	1.37
	aqueous	carboxyl	$\sigma$ bond	O-H	carboxyl	$\pi$ antibond	C=O	$\sigma$ to $\pi^*$	1.36
Ct	gas	carboxyl	$\sigma$ bond	O-H	carboxyl	$\pi$ antibond	C=O	$\sigma$ to $\pi^*$	1.20
	aqueous	carboxyl	$\sigma$ bond	O-H	carboxyl	$\pi$ antibond	C=O	$\sigma$ to $\pi^*$	1.29
enol <sub>a</sub>	gas	carboxyl	lone pair	O	alcohol	$\sigma$ antibond	O-H	$p$ to $\sigma^*$	2.66
		carboxyl	$\sigma$ bond	O-H	carboxyl	$\pi$ antibond	C=O	$\sigma$ to $\pi^*$	1.33
	aqueous	carboxyl	lone pair	O	alcohol	$\sigma$ antibond	O-H	$p$ to $\sigma^*$	2.21
		carboxyl	$\sigma$ bond	O-H	carboxyl	$\pi$ antibond	C=O	$\sigma$ to $\pi^*$	1.35
enol <sub>b</sub>	gas	carboxyl	lone pair	O	alcohol	$\sigma$ antibond	O-H	$p$ to $\sigma^*$	3.86
	aqueous	carboxyl	lone pair	O	alcohol	$\sigma$ antibond	O-H	$p$ to $\sigma^*$	2.57
enol <sub>d</sub>	gas	carboxyl	$\sigma$ bond	O-H	carboxyl	$\pi$ antibond	C=O	$\sigma$ to $\pi^*$	1.30
	aqueous	carboxyl	$\sigma$ bond	O-H	carboxyl	$\pi$ antibond	C=O	$\sigma$ to $\pi^*$	1.37
enol <sub>e</sub>	gas	carboxyl	$\sigma$ bond	O-H	carboxyl	$\pi$ antibond	C=O	$\sigma$ to $\pi^*$	1.35
	aqueous	carboxyl	$\sigma$ bond	O-H	carboxyl	$\pi$ antibond	C=O	$\sigma$ to $\pi^*$	1.39
enol <sub>f</sub>	gas	alcohol	lone pair	O	carboxyl	$\sigma$ antibond	O-H	$p$ to $\sigma^*$	2.38
	aqueous	alcohol	lone pair	O	carboxyl	$\sigma$ antibond	O-H	$p$ to $\sigma^*$	2.26
PAHT <sub>c</sub>	aqueous	carboxylate	lone pair	O	alcohol	$\sigma$ antibond	O-H	$p$ to $\sigma^*$	2.52



**Scheme 1** Reaction pathways of pyruvic acid (PA) decomposition in aqueous phase. Indicated in each arrow are the corresponding transition states based on Fig. 2.

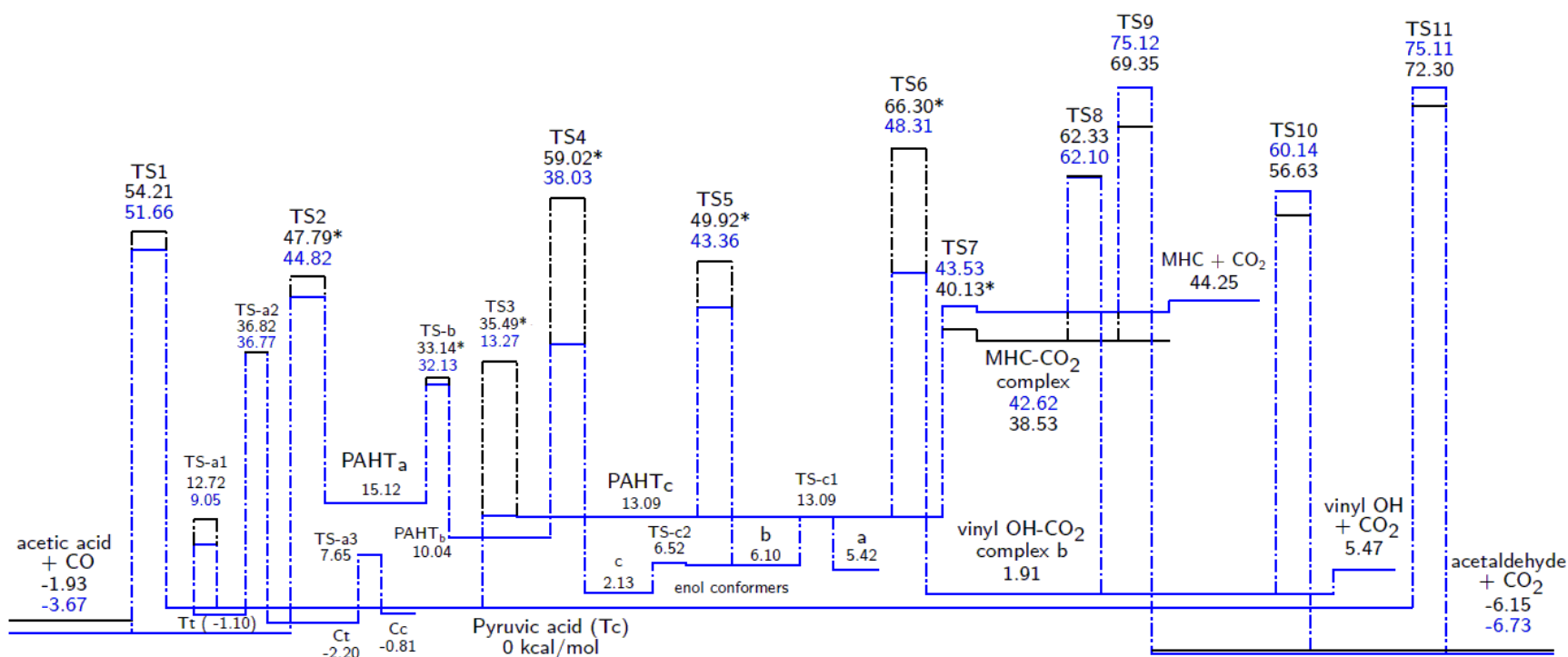


**Fig. 2** Potential energy surface (PES) for the isomerization and decomposition of pyruvic acid (PA) in aqueous phase (blue), calculated at SMD-CCSD(T)-F12/aug-cc-pVDZ-F12//SMD-B2PLYP-D3BJ/aug-cc-pVTZ level of theory. Energies are 0 K enthalpies in kcal/mol, relative to Tc. Previous gas phase energy barriers (black) for major pathways are included for comparison.<sup>44</sup> Barriers with asterisk (\*) goes to a lactone isomers (TS2, TS-b, TS3 and TS4) or directly to Tc (TS5, TS6 and TS7) in gas phase.

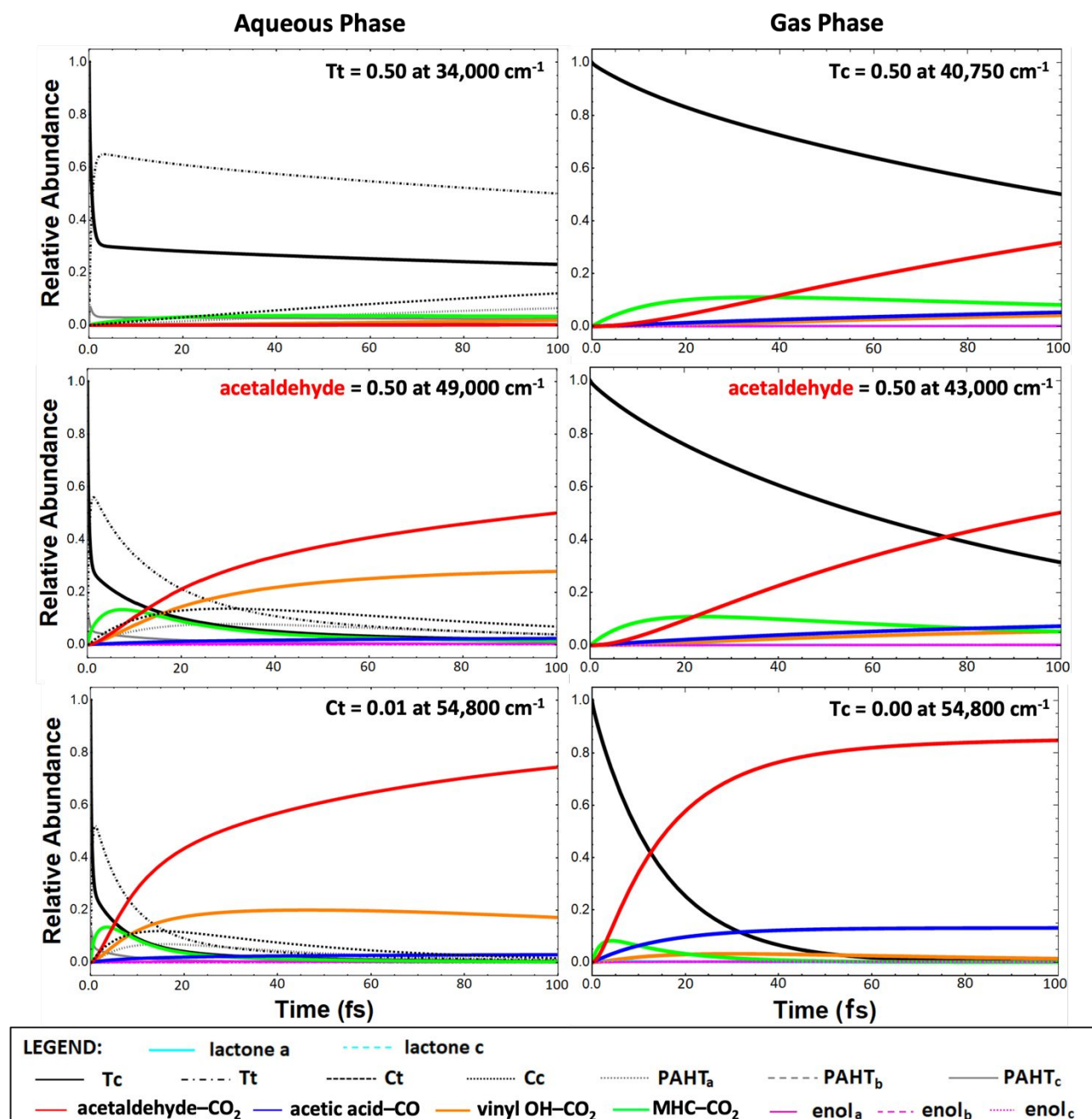


**Fig. 3** Comparison of the temporal dependence of pyruvic acid (PA) degradation species concentration in gas (right)<sup>44</sup> and aqueous phase (left), calculated from RRKM microcanonical coefficients using CCSD(T)-F12/aug-cc-pVDZ-F12 single point energies and B2PLYP-D3BJ/aug-cc-pVTZ frequencies. SMD was used for the aqueous phase calculations. Top panel shows dominant PA conformer abundance at 0.50, middle panel shows dominant product, acetaldehyde, at 0.50, and bottom panel shows PA conformers near zero consumption, all at 100 fs.

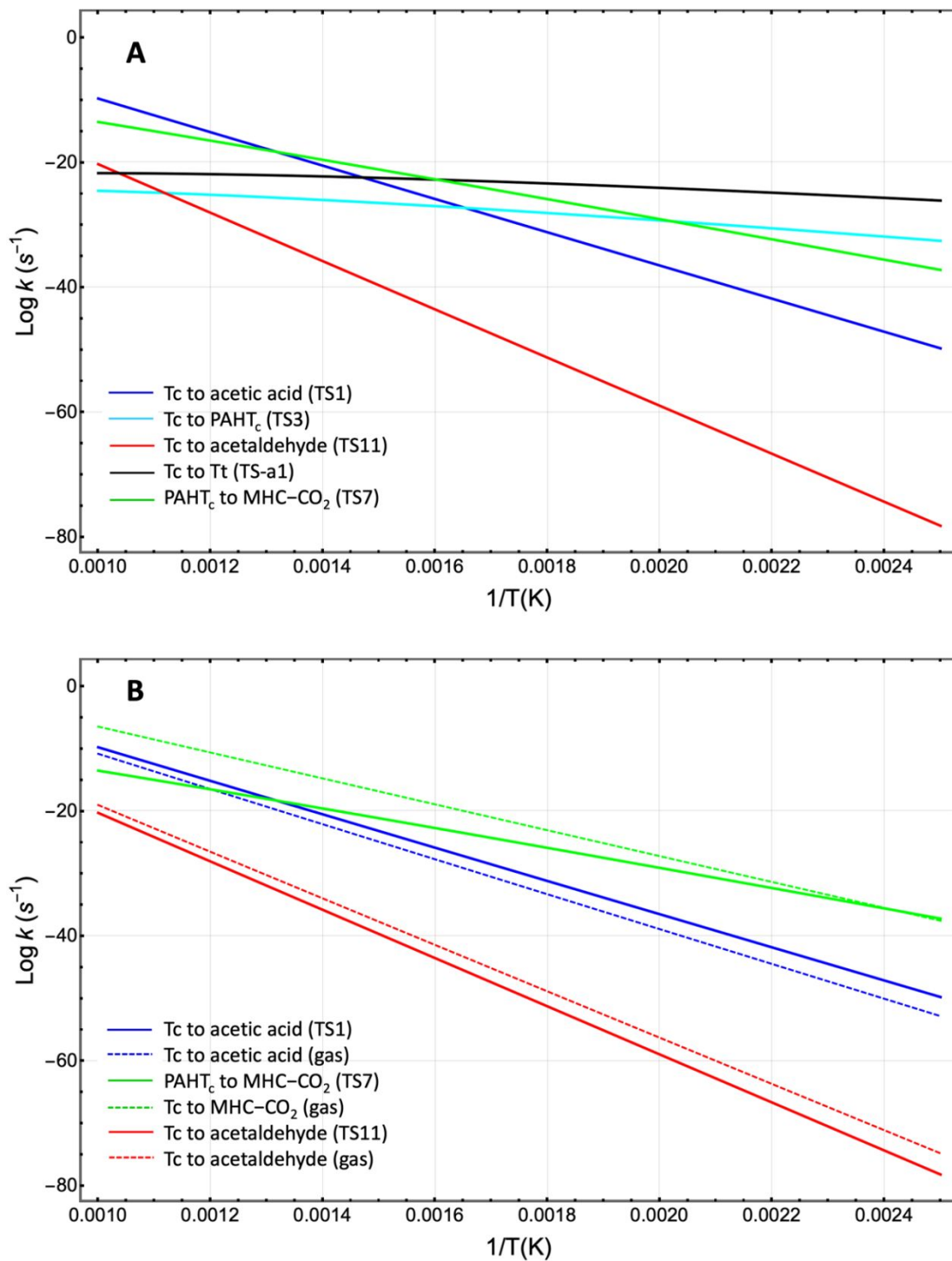


**Fig. 4** Three-parameter fit Arrhenius plots of the RRKM rate coefficients for PA decomposition, calculated from SMD-CCSD(T)-F12/aug-cc-pVDZ-F12 single point energies and SMD-B2PLYP-D3BJ/aug-cc-pVTZ frequencies. Panel A is the comparison of the rates of the main reaction channels in aqueous phase and panel B is the comparison of aqueous and gas phase rates.<sup>44</sup>

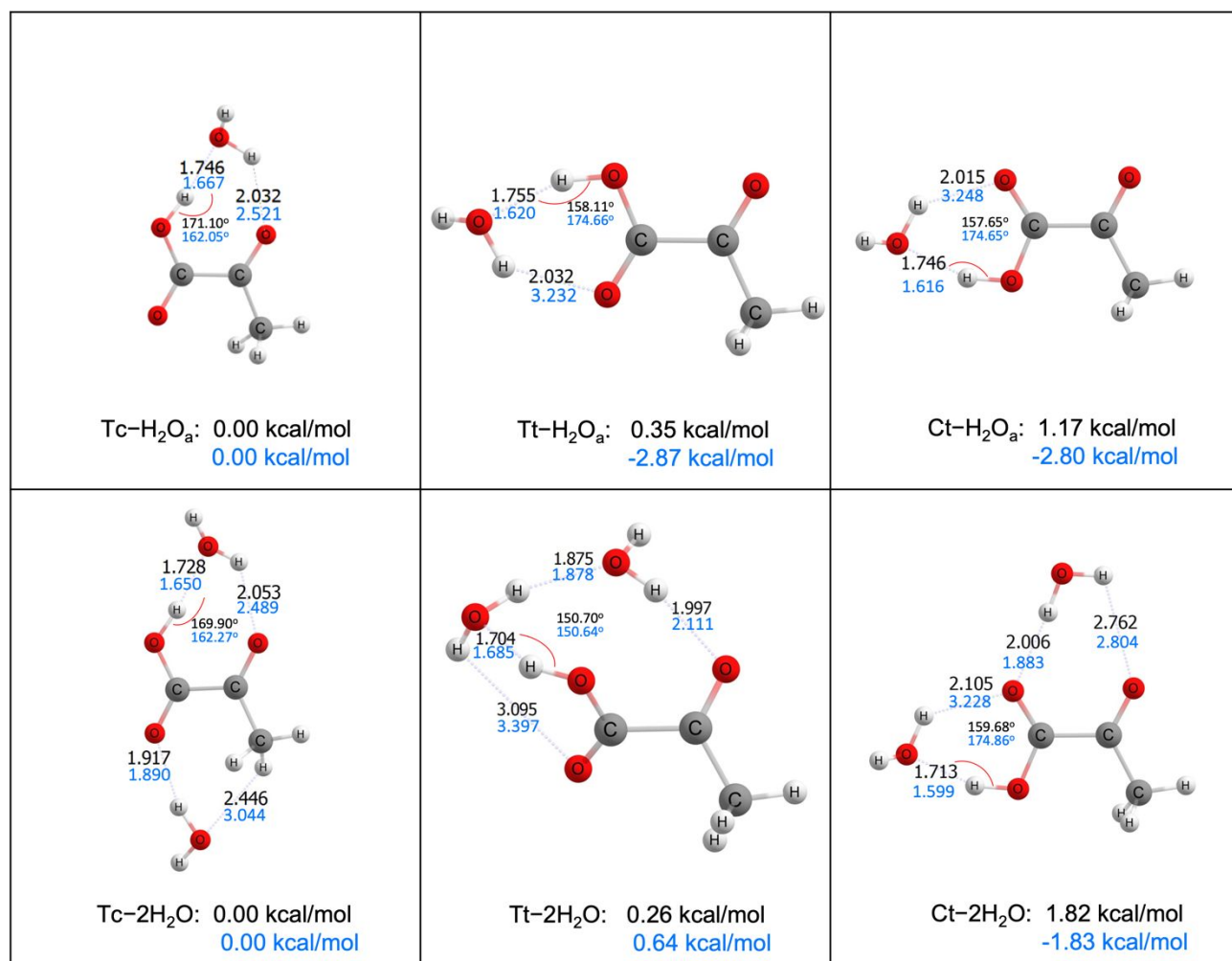


**Fig. 5** Structures of the lowest energy mono- and dihydrated complexes of pyruvic acid (PA) conformers with intra- and intermolecular H-bond distances in Å and OH-O angles in gas (black) and aqueous (blue) phase, calculated at B2PLYP-D3BJ/aug-cc-pVTZ level of theory. Relative  $G^\circ$  are calculated using CCSD(T)-F12/aug-cc-pVDZ-F12. SMD was used for aqueous phase calculations.

**Table 2** Geometric features and major NBO interactions of the lowest energy PA-water complexes containing intermolecular H-bonds in gas and aqueous phase (Fig. 5), calculated at B2PLYP-D3BJ/aug-cc-pVTZ level of theory. Relative  $G^\circ$  are calculated using CCSD(T)-F12/aug-cc-pVDZ-F12. SMD was used for aqueous phase calculations. Highlighted values indicate stronger type of H-bonding.

Complex	H-bond location (e <sup>-</sup> Donor – Acceptor)	Orbital interaction			Bond length, Å		$\Delta$ distance, <sup>a</sup> Å	OH-O angles		relative $G^\circ$ (kcal/mol)	
		Type	Stabilization Energy (kcal/mol)		Gas	Aq		Gas	Aq	Gas	Aq
			Gas	Aq							
<b>PA-H<sub>2</sub>O</b>											
Tc-H <sub>2</sub> O <sub>a</sub>	O <sub>water</sub> – OH <sub>carboxyl</sub>	p to $\sigma^*$	20.67	30.56	1.746	1.667	-0.079	171.10	162.05	0.00	0.00
	O <sub>carbonyl</sub> – OH <sub>water</sub>	p to $\sigma^*$	1.44	0.09	2.032	2.521	0.489	131.07	103.65		
Ct-H <sub>2</sub> O <sub>a</sub>	O <sub>water</sub> – OH <sub>carboxyl</sub>	p to $\sigma^*$	20.30	38.17	1.746	1.616	-0.130	157.65	174.65	1.17	-2.80
	O <sub>carboxyl</sub> – OH <sub>water</sub>	p to $\sigma^*$	4.03	--	2.015	3.248	1.233	134.33	90.77		
Tt-H <sub>2</sub> O <sub>a</sub>	O <sub>water</sub> – OH <sub>carboxyl</sub>	p to $\sigma^*$	19.51	37.48	1.755	1.620	-0.135	158.11	174.66	0.35	-2.87
	O <sub>carboxylic</sub> – OH <sub>water</sub>	p to $\sigma^*$	3.59	--	2.032	3.232	1.200	133.78	91.05		
<b>PA-2H<sub>2</sub>O</b>											
Tc-2H <sub>2</sub> O	O <sub>water1</sub> – OH <sub>carboxyl</sub>	p to $\sigma^*$	22.37	32.86	1.728	1.650	-0.078	169.90	162.27	0.00	0.00
	O <sub>carbonyl</sub> – OH <sub>water1</sub>	p to $\sigma^*$	1.24	0.08	2.053	2.489	0.436	128.72	105.93		
	O <sub>carboxyl</sub> – HO <sub>water2</sub>	p to $\sigma^*$	3.58	4.37	1.917	1.890	-0.027	164.49	177.87		
	O <sub>water2</sub> – HC <sub>methyl</sub>	p to $\sigma^*$	0.52	--	2.446	3.044	0.598	127.89	106.05		
Ct-2H <sub>2</sub> O	O <sub>water1</sub> – OH <sub>carboxyl</sub>	p to $\sigma^*$	23.46	40.92	1.713	1.599	-0.114	159.68	174.86	1.82	-1.83
	O <sub>carboxyl</sub> – HO <sub>water1</sub>	p to $\sigma^*$	2.28	--	2.105	3.228	1.123	128.45	90.89		
	O <sub>carbonyl</sub> – HO <sub>water2</sub>	p to $\sigma^*$	0.05	--	2.762	2.804	0.042	110.24	103.48		
	O <sub>carboxyl</sub> – HO <sub>water2</sub>	p to $\sigma^*$	3.06	6.80	2.006	1.883	-0.123	175.71	166.60		
Tt-2H <sub>2</sub> O	O <sub>water1</sub> – OH <sub>carboxyl</sub>	p to $\sigma^*$	25.96	27.73	1.704	1.685	-0.019	150.70	150.64	0.26	0.64
	HO <sub>water1</sub> – O <sub>carboxyl</sub>	$\sigma$ to $\pi^*$	0.10	0.10	3.095	3.397	0.302	94.86	83.79		
	O <sub>carbonyl</sub> – HO <sub>water2</sub>	p to $\sigma^*$	4.68	2.81	1.997	2.111	0.114	164.91	169.55		
	O <sub>water1</sub> – HO <sub>water2</sub>	p to $\sigma^*$	9.10	10.80	1.875	1.878	0.003	159.39	160.93		

<sup>a</sup> Change in H-bond length from gas to aqueous phase:  $\Delta$ distance = Distance<sub>aq</sub> - Distance<sub>gas</sub>

**Table 3** Relative thermodynamic properties (in kcal/mol) of pyruvic acid (PA) conformers and their hydrates, with respect to their Tc forms, in gas and aqueous phase. Calculations were done at 1 atm and 298.15 K using CCSD(T)-F12/aug-cc-pVDZ-F12//B2PLYP-D3BJ/aug-cc-pVTZ level of theory. SMD was used for aqueous phase calculations.

Species		Gas phase			Aqueous phase		
		rel. $H^{\circ}_{\text{gas}}$	rel. $-TS^{\circ}_{\text{gas}}$	rel. $G^{\circ}_{\text{gas}}$	rel. $H^{\circ}_{\text{aq}}$	rel. $-TS^{\circ}_{\text{aq}}$	rel. $G^{\circ}_{\text{aq}}$
PA monomers	Tc	0.00	0.00	0.00	0.00	0.00	0.00
	Ct	4.28	-0.88	3.40	-2.15	-0.10	-2.25
	Tt	2.75	-0.36	2.39	-1.05	-0.14	-1.20
	Cc	--	--	--	-0.79	0.02	-0.77
PA-H <sub>2</sub> O complexes	Tc-H <sub>2</sub> O <sub>a</sub>	0.00	0.00	0.00	0.00	0.00	0.00
	Ct-H <sub>2</sub> O <sub>a</sub>	1.07	0.10	1.17	-2.28	-0.52	-2.80
	Tt-H <sub>2</sub> O <sub>a</sub>	0.19	0.16	0.35	-2.34	-0.52	-2.87
PA-2H <sub>2</sub> O complexes	Tc-2H <sub>2</sub> O	0.00	0.00	0.00	0.00	0.00	0.00
	Ct-2H <sub>2</sub> O	1.59	0.23	1.82	-2.80	0.97	-1.83
	Tt-2H <sub>2</sub> O	-1.03	1.30	0.26	0.53	0.11	0.64

**Table 4** Thermodynamics of water complexation (in kcal/mol) of pyruvic acid (PA) conformers in gas and aqueous phase. Calculations were done at 1 atm and 298.15 K, using CCSD(T)-F12/aug-cc-pVDZ-F12//B2PLYP-D3BJ/aug-cc-pVTZ level of theory. SMD was used for aqueous phase calculations.

Species	Explicit hydration in gas phase			Explicit hydration in aqueous phase			
	$\Delta H_{\text{gas}}^{\circ}$	$-T\Delta S_{\text{gas}}^{\circ}$	$\Delta G_{\text{gas}}^{\circ}$	$\Delta H_{\text{aq}}$	$-T\Delta S_{\text{aq}}$	$\Delta G_{\text{aq}}$	$\Delta G_{\text{aq}}^{\circ a}$
PA-H <sub>2</sub> O complexes							
H <sub>2</sub> O + Tc → Tc-H <sub>2</sub> O <sub>a</sub>	-7.13	9.19	2.06	-4.88	9.41	4.52	2.63
H <sub>2</sub> O + Ct → Ct-H <sub>2</sub> O <sub>a</sub>	-10.34	10.17	-0.17	-5.01	8.99	3.98	2.09
H <sub>2</sub> O + Tt → Tt-H <sub>2</sub> O <sub>a</sub>	-9.69	9.70	0.01	-6.17	9.03	2.85	0.96
PA-2H <sub>2</sub> O complexes							
H <sub>2</sub> O + Tc-H <sub>2</sub> O <sub>a</sub> → Tc-2H <sub>2</sub> O	-5.84	8.03	2.19	2.04	8.63	10.68	8.79
H <sub>2</sub> O + Ct-H <sub>2</sub> O <sub>a</sub> → Ct-2H <sub>2</sub> O	-5.32	8.16	2.84	1.52	10.12	11.64	9.75
H <sub>2</sub> O + Tt-H <sub>2</sub> O <sub>a</sub> → Tt-2H <sub>2</sub> O	-7.07	9.18	2.11	4.91	9.26	14.18	12.29

<sup>a</sup> Change in Gibbs free energy in aqueous phase, corrected with the conversion between standard states (gas to aqueous phase:  $G^{\circ}_{\text{conc}} = 1.89$  kcal/mol):

where  $\Delta G^{\circ}_{\text{aq}} = G^{\circ}_{\text{aq}}(\text{Product}) - G^{\circ}_{\text{aq}}(\text{Reactant})$

$G^{\circ}_{\text{aq}}(\text{Product}) = H^{\circ}_{\text{aq}} - TS^{\circ}_{\text{aq}} + G^{\circ}_{\text{conc}}$

$G^{\circ}_{\text{aq}}(\text{Reactant}) = H^{\circ}_{\text{aq}} - TS^{\circ}_{\text{aq}} + G^{\circ}_{\text{conc}}$

**Table 5** Thermodynamics of covalent hydration (in kcal/mol) of pyruvic acid (PA) to 2,2-dihydroxypropanoic acid (DHPA) and PA-water complexes to DHPA–H<sub>2</sub>O in gas and aqueous phase. Calculations were done at 1 atm and 298.15 K, using CCSD(T)-F12/aug-cc-pVDZ-F12//B2PLYP-D3BJ/aug-cc-pVTZ level of theory. SMD was used for aqueous phase calculations. Values in parentheses (\*) are for Tc–H<sub>2</sub>O<sub>a</sub>' and Tc–H<sub>2</sub>O<sub>b</sub> in gas and aqueous phase, respectively.

Reaction	Explicit hydration in gas phase			Explicit hydration in aqueous phase			
	$\Delta H_{\text{gas}}^{\circ}$	$-T\Delta S_{\text{gas}}^{\circ}$	$\Delta G_{\text{gas}}^{\circ}$	$\Delta H_{\text{aq}}$	$-T\Delta S_{\text{aq}}$	$\Delta G_{\text{aq}}$	$\Delta G_{\text{aq}}^{\circ a}$
Monohydration							
H <sub>2</sub> O + Tc → Tc–H <sub>2</sub> O <sub>a</sub> (*)	-7.13 (-5.66)	9.19 (8.54)	2.06 (2.88)	-4.88 (-2.87)	9.41 (8.36)	4.53 (5.49)	2.64 (3.6)
Tc–H <sub>2</sub> O <sub>a</sub> (*) → DHPA	-1.15 (-2.62)	2.75 (3.40)	1.60 (0.78)	4.53 (2.51)	2.97 (4.02)	7.50 (6.53)	7.50 (6.53)
H <sub>2</sub> O + Tc → DHPA	-8.28	11.94	3.66	-0.35	12.38	12.03	10.14
Dihydration							
H <sub>2</sub> O + Tc–H <sub>2</sub> O <sub>a</sub> → Tc–2H <sub>2</sub> O	-5.84	8.03	2.19	2.04	8.63	10.67	8.78
Tc–2H <sub>2</sub> O → DHPA–H <sub>2</sub> O	-3.86	4.74	0.88	-3.08	3.74	0.66	0.66
H <sub>2</sub> O + Tc–H <sub>2</sub> O <sub>a</sub> → DHPA–H <sub>2</sub> O	-9.70	12.77	3.07	-1.04	12.37	11.33	9.44
H <sub>2</sub> O + DHPA → DHPA–H <sub>2</sub> O	-8.55	10.03	1.48	-5.57	9.40	3.83	1.94

<sup>a</sup> Change in Gibbs free energy in aqueous phase, corrected with the conversion between standard states (gas to aqueous phase:  $G_{\text{conc}}^{\circ} = 1.89$  kcal/mol):

where  $\Delta G_{\text{aq}}^{\circ} = G_{\text{aq}}^{\circ}(\text{Product}) - G_{\text{aq}}^{\circ}(\text{Reactant})$

$G_{\text{aq}}^{\circ}(\text{Product}) = H_{\text{aq}}^{\circ} - TS_{\text{aq}}^{\circ} + G_{\text{conc}}^{\circ}$

$G_{\text{aq}}^{\circ}(\text{Reactant}) = H_{\text{aq}}^{\circ} - TS_{\text{aq}}^{\circ} + G_{\text{conc}}^{\circ}$

**Table 6** Activation energies ( $E_a$ ) of 2,2-dihydroxypropanoic acid (DHPA) and DHPA-H<sub>2</sub>O formation in gas and aqueous phase, calculated at SMD-CCSD(T)-F12/aug-cc-pVDZ-F12//SMD-B2PLYP-D3BJ/aug-cc-pVTZ level of theory. Gas phase values are taken from previous calculations.<sup>44</sup>

Medium	Reactant	Product	$E_{\text{rxn}}$ (kcal/mol)	Transition State	$E_a$ (kcal/mol)
gas	Tc-H <sub>2</sub> O <sub>b</sub> '	DHPA	-1.32	TS-DHPA	39.55
aqueous	Tc-H <sub>2</sub> O <sub>b</sub>		4.25		41.83
gas	Tc-2H <sub>2</sub> O	DHPA-H <sub>2</sub> O	-2.14	TS-DHPA-H <sub>2</sub> O	34.33
aqueous			-1.65		37.84

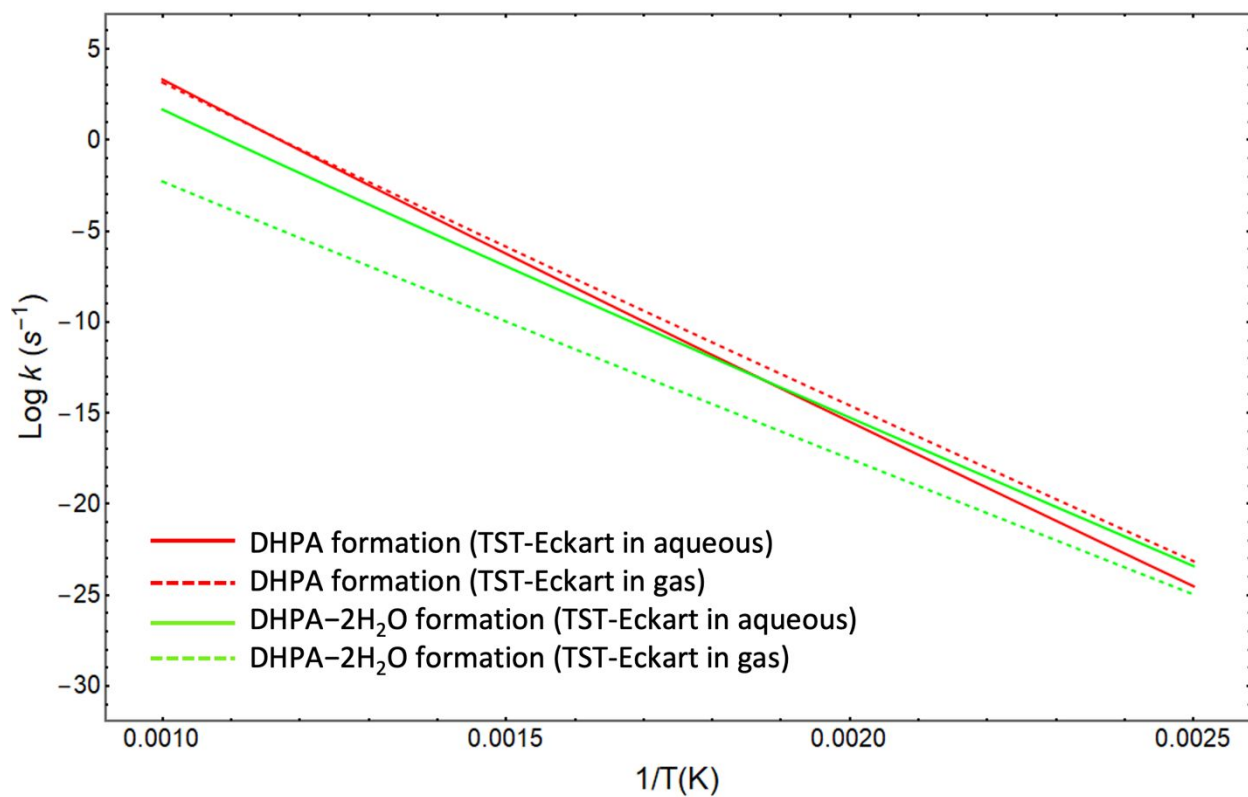


**Fig. 6** Comparison of the Arrhenius plots of the rate coefficients ( $k$ ) for 2,2-dihydroxypropanoic acid (DHPA) and DHPA-H<sub>2</sub>O formation between gas<sup>44</sup> and aqueous phase using TST with Eckart tunneling, calculated from SMD-CCSD(T)-F12/aug-cc-pVDZ-F12 single point energies and SMD-B2PLYP-D3BJ/aug-cc-pVTZ frequencies.